AD-A275 315

IIIIIIIIIIIII

TGAL-93-6

USER'S MANUAL OF FD2: A SOFTWARE PACKAGE FOR MODELING SEISMOLOGICAL PROBLEMS WITH 2-DIMENSIONAL LINEAR FINITE-DIFFERENCE METHOD

Rong-Song Jih

Teledyne Geotech Alexandria Laboratory
3I4 Montgomery Street
Alexandria, Virginia 22314-1581

JULY 1993

DTIC
S ELECTE
FEB 01 1994
E
D

SPECIAL TOPICAL REPORT:	1 May 1993 - 15 July 1993
ARPA ORDER NO.:	6731
PROJECT TITLE:	Statistical Study of Soviet Explosion Magnitudes and Yields Using Heavily Censored Historical Yields, Soviet-released Analog Waveforms, and Digital Data Recorded at Modern Arrays
CONTRACT NO.:	F29601-91-C-DB23

94-03130
IIIIIIIIIIIIIII

94 1 31 222

REPORT DOCUMENTATION PAGE

1. AGENCY USE ONLY (Leave blank)	2. REPORT DATE 15 July 1993	3. REPORT TYPE AND DATES COVERED Speicial Topical Report, 1 May 1993 - 15 July 1993

4. TITLE AND SUBTITLE

User's Mansul of FD2: a Software Package for Modeling Seismological Problems with 2-dimensional Linear Finite-Difference Method

5. FUNDING NUMBERS

Contract F29601-91-C-DB23

PE 62101F
PR 7600
TA 09
WU AT

6. AUTHOR(S)

R.-S. Jih

7. PERFORMING ORGANIZATION NAME(S) AND ADDRESS(ES)

Teledyne Geotech Alexandria Laboratory
314 Montgomery Street
Alexandria, VA 22314-1581

8. PERFORMING ORGANIZATION REPORT NUMBER

TGAL-93-06

9. SPONSORING / MONITORING AGENCY NAME(S) AND ADDRESS(ES)

ARPA/NMRO (Attn. Dr. Alan Ryall)
3701 North Fairfax Drive
Arlington, VA 22203-1714

10. SPONSORING / MONITORING AGENCY REPORT NUMBER

11. SUPPLEMENTARY NOTES

12a. DISTRIBUTION / AVAILABILITY STATEMENT

Approved for Public Release; Distribution Unlimited

12b. DISTRIBUTION CODE

13. ABSTRACT (Maximum 200 words)

"Fd2" is a software package developed at Teledyne Geotech Alexandria Laboratories (TGAL) during the past several years for generating synthetic seismograms and displaying the wavefields. This package consists of primarily a 2-dimensional 2nd-order explicit linear finite-difference (LFD) code. LFD method has the advantage that the solution contains all conversions and all orders of multiple scattering. It permits examinations of fairly general models with arbitrary complex variations in material properties and free-surface geometry. Furthermore, it does not require many assumptions commonly invoked in other theoretical approaches. The basic limitations to the LFD method or the finite-element method are the computational cost and memory requirements. These constrain the size of the grid and the number of time steps that can be calculated over a reasonable time frame. Our LFD code has a distinguishable feature in that it allows the inclusion of topographical free surface. This is particularly useful in modeling nuclear explosions buried in mountains.

In this topical report, sample scripts are presented to illustrate the usage of "fd2" and several supporting routines for plotting out the synthetics, generating 2-dimensional media, as well as the graphic visualization of wavefields. The algorithms for handling the boundary conditions of polygonal topography are reviewed in detail. Thus this topical report serves as both a programmer's guide and the user's manual.

14. SUBJECT TERMS

Numerical Modeling, Finite-difference Method, Free-surface Topography, Seismic Waves, Propagation, Scattering, Ripple Firing

15. NUMBER OF PAGES

16. PRICE CODE

17. SECURITY CLASSIFICATION OF REPORT	18. SECURITY CLASSIFICATION OF THIS PAGE	19. SECURITY CLASSIFICATION OF ABSTRACT	20. LIMITATION OF ABSTRACT
Unclassified	Unclassified	Unclassified	UL

(THIS PAGE INTENTIONALLY LEFT BLANK)

SUMMARY

"Fd2" is a software package developed at Teledyne Geotech Alexandria Laboratories (TGAL) during the past several years for generating synthetic seismograms and displaying the wavefields. This package consists of primarily a 2-dimensional 2nd-order explicit linear finite-difference (LFD) code. LFD method has the advantage that the solution contains all conversions and all orders of multiple scattering. It permits examinations of fairly general models with arbitrary complex variations in material properties and free-surface geometry. Furthermore, it does not require many assumptions commonly invoked in other theoretical approaches. The basic limitations to the LFD method or the finite-element method are the computational cost and memory requirements. These constrain the size of the grid and the number of time steps that can be calculated over a reasonable time frame. Our LFD code has a distinguishable feature in that it allows the inclusion of topographical free surface. This is particularly useful in modeling nuclear explosions buried in mountains.

In this topical report, sample scripts are presented to illustrate the usage of "fd2" and several supporting routines for plotting out the synthetics, generating 2-dimensional media, as well as the graphic visualization of wavefields. The algorithms for handling the boundary conditions of polygonal topography are reviewed in detail. Thus this topical report serves as both a programmer's guide and the user's manual.

Accesion For		
NTIS CRA&I	☒	
DTIC TAB	☐	
U..announced	☐	
Justification _____		
By _____		
Dist.ibution /		
Availability Codes		
Dist	Avail and / or Special	
A-1		

DTIC QUALITY INSPECTED 5

(THIS PAGE INTENTIONALLY LEFT BLANK)

Table of Contents

(THIS PAGE INTENTIONALLY LEFT BLANK)

1. INTRODUCTION

Wave propagation problems in seismology involve the solution of a set of differential equations in a medium in which the material properties vary in space, *i.e.*, the earth. The use of numerical simulations is a straightforward means for studying this kind of problem especially when laterally-varying velocity structure or complex topographic relief is encountered. Methods such as Gaussian beam technique and ray theoretical schemes are restricted to cases where variations of the medium are much larger than the seismic wavelength. The Kirchhoff-Helmholtz integration method is useful for media with sharp interfaces, but it does not include the multiple scattering along the interfaces, and it is not appropriate for reflections from velocity gradients similar in extent to the seismic wavelength. Perturbation methods are applicable only for weak scattering problems. Among all numerical approaches, finite-difference (FD) and finite-element (FE) methods are not restricted to velocity variations of a particular size with respect to wavelength. FD and FE can generate synthetic seismograms for very complicated media in cases of weak/strong or multiple scattering.

FD method solves either the wave equations or the elastodynamic equations by replacing the partial derivatives in space and time by their finite-difference approximations. When explicit FD method is used, which is the most popular FD technique to date, the wavefield of a specific time instant is solved one grid point by one grid point with nearby grid data at previous steps. For schemes that use second-order approximations to the temporal derivative, only two grid planes of displacement (or stress, velocity) must be stored to perform the updating process. Once the entire grid is updated, FD then proceeds to compute the wavefield of the next time instant until a certain preselected number of iterations is reached. The output of FD method can be snapshots of the entire grid at specific times or synthetic seismograms recorded at specific grid points.

"Fd2" is a software package developed at Teledyne Geotech Alexandria Laboratories (TGAL) during the past several years for generating synthetic seismograms and displaying the wavefields. This package consists mainly of a 2-dimensional 2nd-order explicit linear finite-difference (LFD) code. In this topical report, we first review in detail the algorithms we developed for the topography handling. We then present sample scripts illustrating the usage of *"fd2"* as well as several supporting routines for plotting out the synthetics, generating media, and the graphic visualization of wavefields. Thus this topical report serves as both a programmer's guide and the user's manual. The supporting routines included in this manual are *"fd_menu"*, *"fdsplt"*, *"arrayplt"*, *"trplt"*, *"movie"*, and *"tymed3"*, which constitute the most frequently used portion of our software package.

Although LFD codes are becoming very popular, our code does posses several features that are not that standard. Perhaps the most distinguishable feature of this code is that it allows simulations with fairly rough topography. Topography can focus or defocus incident body waves and can convert body waves to surface waves and *vice versa*. In this tutorial we therefore include an overview of our topography algorithms which are based largely on our published work (Jih *et al.*, 1988). Basically the algorithm we developed is an improved version of Ilan (1977). On the inclined free-surface, the vanishing stress conditions are implemented to a rotated coordinate system parallel to the inclined boundary as previous works did. For each transition point on the topography where the slope changes, we use the first-order approximation of boundary conditions in a locally rotated coordinate system in which the normal axis

always coincides with the bisector of the corner. These extrapolation formulae are consistent with boundary conditions to first-order accuracy in spatial increment, the same as the classical one-sided explicit approximation scheme widely used for the flat free-surface case. Testing results indicate that this scheme works stably for fairly complicated geometric shapes consisting of ridges and valleys with steep and gentle slopes over a range of Poisson ratios of practical interest, thus enabling us to study more realistic problems for which the topography plays a significant role in shaping the wavefield and analytical solution might not be available.

A few words on the evolving history of Geotech's LFD code are necessary: Z. A. Der, J. Burnetti, and T. McElfresh initialized the prototype code design in late seventies. During 1978-1981, they implemented the 2nd-order explicit FD scheme with the heterogeneous formulation of Kelly *et al.* (1976), the monochromatic *P/SV* planar source, as well as the symmetric boundary condition. K. L. McLaughlin, T. McElfresh, and L. Anderson implemented Ohnaka (broadband) *P/SV* source, the point (line) source and the absorbing boundary condition (Clayton and Engquist, 1977; Emerman and Stephen, 1983) during 1983-1985. R.-S. Jih coded up the fundamental-mode Rayleigh wave generation routine (Boore, 1970; Munasinghe and Farnell, 1973), the 1st-order formulation of free-surface boundary condition to handle the polygonal topography (Jih *et al.*, 1988), the marching grid technique for extending the propagation distance in the lateral direction (Jih *et al.*, 1989), as well as a strain filter for far-field body wave synthetics (Jih *et al.*, 1989). The current version of FD code *"fd2"* is totally different from all earlier versions of Geotech's LFD codes: *("fdabc1"* through *"fdabc6")* after a series of heavy revisions by R.-S. Jih during 1986-1993, even though several subroutines still retain their original names.

2. TOPOGRAPHIC ALGORITHMS

2.1 Basic Concepts Underlying Topographic Algorithms

Consider a half-space with an arbitrary polygonal free-surface. Define a Cartesian coordinate system with X horizontal (positive to the right) and Z vertical (positive downward) as in Figure 1. Assume that the material is perfectly elastic, isotropic, and homogeneous with compressional and shear velocities α and β respectively. Let U and W be the X and Z components of displacement. Then the wave propagation at interior points is governed by the following hyperbolic partial differential equations:

$$\frac{\partial^2 U(x,z,t)}{\partial t^2} = \alpha^2 \frac{\partial^2 U(x,z,t)}{\partial x^2} + (\alpha^2 - \beta^2) \frac{\partial^2 W(x,z,t)}{\partial x \partial z} + \beta^2 \frac{\partial^2 U(x,z,t)}{\partial z^2} \qquad [1a]$$

and

$$\frac{\partial^2 W(x,z,t)}{\partial t^2} = \alpha^2 \frac{\partial^2 W(x,z,t)}{\partial x^2} + (\alpha^2 - \beta^2) \frac{\partial^2 U(x,z,t)}{\partial x \partial z} + \beta^2 \frac{\partial^2 W(x,z,t)}{\partial z^2} . \qquad [1b]$$

A grid is imposed on the X-Z plane with fixed mesh size Δx and Δz . We let $x = i\Delta x$, $z = k\Delta z$, and $t = l\Delta t$, where Δt is the increment step in time, and i, k, and l are positive integers. We denote by $U_{i,k,l}$ and $W_{i,k,l}$ the components of displacement at the discretized grid point $<i,k> = (i\Delta x, k\Delta z, l\Delta t)$ at the lth time step. By replacing the partial derivatives in equation [1] by central differences, the following standard explicit second-order formulae are obtained:

$$U_{i,k,l+1} = - U_{i,k,l-1} + 2U_{i,k,l} + \alpha^2 (\frac{\Delta t}{\Delta x})^2 (U_{i+1,k,l} - 2U_{i,k,l} + U_{i-1,k,l})$$

$$+ \beta^2 (\frac{\Delta t}{\Delta z})^2 (U_{i,k+1,l} - 2U_{i,k,l} + U_{i,k-1,l})$$

$$+ \frac{1}{4} \frac{\Delta t^2}{\Delta x \Delta z}(\alpha^2 - \beta^2) . (W_{i+1,k+1,l} - W_{i+1,k-1,l} - W_{i-1,k+1,l} + W_{i-1,k-1,l}) \qquad [1c]$$

and

$$W_{i,k,l+1} = - W_{i,k,l-1} + 2W_{i,k,l} + \alpha^2 (\frac{\Delta t}{\Delta z})^2 (W_{i,k+1,l} - 2W_{i,k,l} + W_{i,k-1,l})$$

$$+ \beta^2 (\frac{\Delta t}{\Delta x})^2 (W_{i+1,k,l} - 2W_{i,k,l} + W_{i-1,k,l})$$

$$+ \frac{1}{4} \frac{\Delta t^2}{\Delta x \Delta z}(\alpha^2 - \beta^2) . (U_{i+1,k+1,l} - U_{i+1,k-1,l} - U_{i-1,k+1,l} + U_{i-1,k-1,l}) . \qquad [1d]$$

The reader is referred to Alterman and Karal (1968), Boore (1972), and Kelly et al. (1976) for a more detailed discussion of the approximation of partial derivatives by finite difference discretizations.

The vanishing of stress on the flat free-surface boundary is expressed by $\tau_{xz} = 0$ and $\tau_{zz} = 0$, or, equivalently,

3

$$\frac{\partial U}{\partial z} + \frac{\partial W}{\partial x} = 0 \tag{2a}$$

and

$$\frac{\partial W}{\partial z} + (1 - 2\frac{\beta^2}{\alpha^2})\frac{\partial U}{\partial x} = 0 . \tag{2b}$$

Alterman and Karal (1968) presented an explicit central-difference approximation of [2a, b] which is stable when $\beta/\alpha > 0.3$:

$$U_{i,k} = U_{i,k+2} - \frac{\Delta z}{\Delta x} (W_{i+1,k+1} - W_{i-1,k+1}) \tag{2c}$$

and

$$W_{i,k} = W_{i,k+2} - \frac{\Delta z}{\Delta x} (1 - 2\frac{\beta^2}{\alpha^2})(U_{i+1,k+1} - U_{i-1,k+1}) . \tag{2d}$$

Another approach which adopts one-sided differences was proposed by Alterman and Rotenberg (1969):

$$U_{i,k} = U_{i,k+1} - \frac{\Delta z}{2\Delta x} (W_{i+1,k+1} - W_{i-,k-1}) \tag{2e}$$

and

$$W_{i,k} = W_{i,k+1} - \frac{\Delta z}{2\Delta x} (1 - 2\frac{\beta^2}{\alpha^2})(U_{i+1,k+1} - U_{i-1,k-1}) . \tag{2f}$$

At the vertical surface the boundary values can be derived by the following transformations:

$$U \longrightarrow W, W \longrightarrow U, \partial x \longrightarrow \partial z, \partial z \longrightarrow \partial x. \tag{3}$$

Although the one-sided approximation [2e,f] is applicable over a somewhat more restrictive range of Poisson's ratios, in some cases results are even better than the central-difference approximation [2c,d] or a composed second-order scheme by Ilan and Loewenthal (1976). All algorithms discussed in later sections will use either equations [2c,d] or equations [2e,f].

Alterman and Loewenthal (1970) proposed two approaches to the calculation of the displacements at 90° and 270° corners. The first approach requires that the normal stress components on both the horizontal and the vertical surface be zero, and in place of condition [2a], it imposes a more restrictive condition of $\partial U/\partial x = \partial W/\partial z = 0$. The second approach smooths the corner slightly, making the tangent to the boundary be at an angle of 45° to both axes. Two similar difference schemes following the second approach can be found in Ilan et al. (1975) and Fuyuki and Matsumoto (1980). Boore et al. (1981) reported that Fuyuki and Matsumoto's difference equations are somewhat better. We will follow the idea of the second approach to derive formulations for arbitrary corners.

To implement arbitrary topography in the 2-dimensional finite-difference scheme, it suffices to approximate the topography by polygons. Six algorithms are presented here to implement the free-surface boundary condition for the six separate cases shown in Figure 1 labeled (A) through (F). Only

4

the formulae for increasing elevation with increasing x are given for brevity. Since the calculation of corner points always requires displacements of points nearby, it is necessary to follow a specific order in each time marching step to solve the boundary values: first compute points on the horizontal and vertical free-surface segments with [2c,..., 2f] (or transformation 3), then points on the ramps, and finally the corner points. The topography is restricted such that each segment of the polygon consists of at least three points, so that corner points are always separated by ramp points (at least one). The selection of spatial sampling increment, Δx and Δz, depends on the velocities, frequencies, and geometric resolution of the problem to be solved. For complicated topography it is necessary to adopt smaller Δz (relative to Δx) to ensure the inclusion of the most gentle ramp encountered, namely the ramp with slope $\Delta z/\Delta x$. The temporal spacing Δt is then determined by the mesh spacings as well as by wave velocities so as to match the general stability constraint.

The underlying procedure for all the six topography algorithms is the following:

(1)   At every node on the topography, set up a rotated coordinate system $X'-Z'$ which accounts for the local geometric orientation. For corner points, simply take the bisector of the corner as the Z' axis. For points on the ramp, this means that Z' is the local normal to the ramp.

(2)   Set up a four-atom molecule with diagonals parallel to the $X'-Z'$ axes and let the unknown node $<i,k>$ be one of the atoms by default. Remaining atoms are selected so that their displacement can be computed with interior points, thus ensuring the scheme remains explicit. The molecule itself should be as close as possible to the boundary to reduce error due to coarse sampling of the wave field. Usually it is convenient to put an atom just one grid below node $<i,k>$.

(3)   Apply equations [2c,d] or equations [2e,f] to the four-atom computational molecule to solve for the boundary value at node $<i,k>$ in the $X'-Z'$ coordinate system. The solution is then rotated back to the original $X-Z$ system.

The details of the various algorithms are presented in Section 2.3.
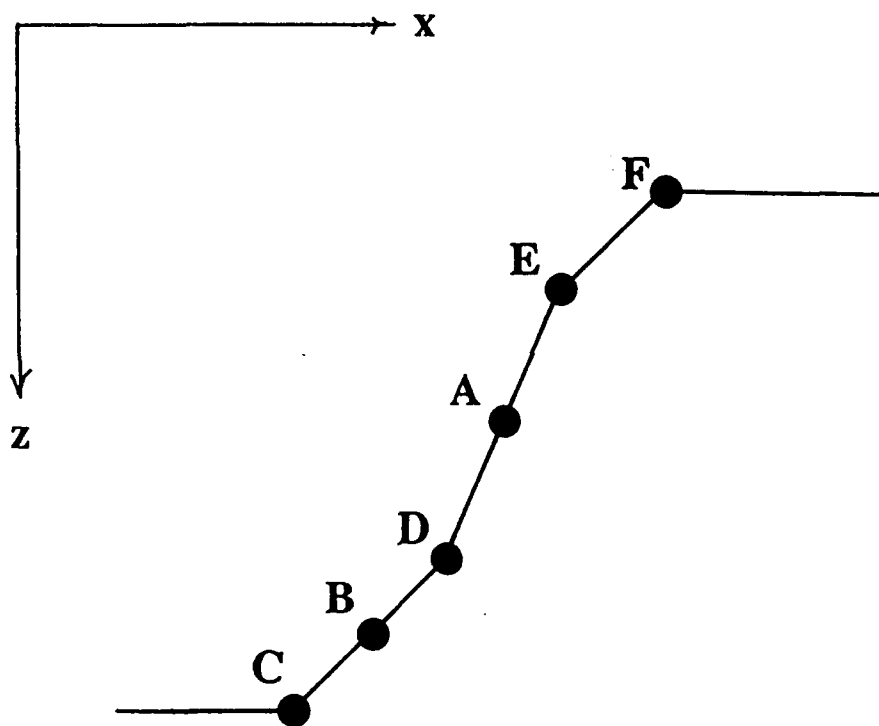
Figure 1

2.2 Ilan's Method for Constant-slope Ramp

Ilan (1977) uses a rectangular grid with fixed height Δz and variable width Δx_i. Each Δx_i is determined via $\Delta x = \Delta z \cot\theta$, where θ is the local angle between the X-direction and the inclined free-surface.

Suppose that node $<i,k>$ lies on an inclined free-surface with slope $\Delta z/\Delta x$ (Figure 2). If $\theta = \tan^{-1}(\Delta z/\Delta x) \leq 45°$, Let

$$U'_{i,k} = U'_0 - \sin2\theta(W'_{i+1,k} - W'_{i,k+1}) \tag{4a}$$

and

$$W'_{i,k} = W'_0 - \sin2\theta(1 - 2\frac{\beta^2}{\alpha^2})(U'_{i+1,k} - U'_{i,k+1}) , \tag{4b}$$

where

$$U_0 = \varepsilon_0 U_{i+1,k+1} + (1 - \varepsilon_0)U_{i,k+2} , \tag{5a}$$

$$W_0 = \varepsilon_0 W_{i+1,k+1} + (1 - \varepsilon_0)W_{i,k+2} , \tag{5b}$$

and

$$\varepsilon_0 = 2\sin^2\theta . \tag{5c}$$

If $\theta \geq 45°$, then replace equations [5] by

$$U_0 = \varepsilon_0 U_{i+1,k+1} + (1 - \varepsilon_0)U_{i+2,k} , \tag{6a}$$

$$W_0 = \varepsilon_0 W_{i+1,k+1} + (1 - \varepsilon_0)W_{i+2,k} , \tag{6b}$$

and

$$\varepsilon_0 = 2\cos^2\theta . \tag{6c}$$

Finally rotate $U'_{i,k}$, $W'_{i,k}$ of equations [4] back to the original system.

We have observed that without appropriate manipulation of the transition points on the topography as proposed in the present work, this algorithm alone would suffer from instabilities. Furthermore, this *single algorithm with varying grid spacing* approach yields more complexity in its use than does the *multi-algorithm with fixed grid spacing* described in the present work.
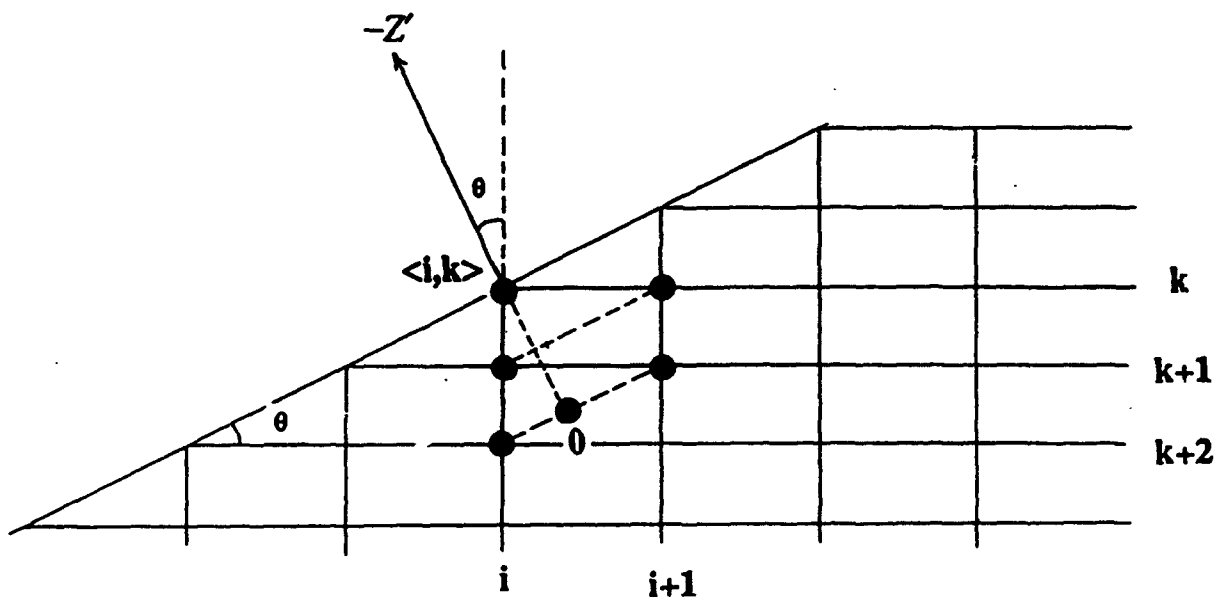
Figure 2

2.3 Algorithms Used in FD2

(A) Constant Steep Slope

Suppose that a grid point <i,k> lies on an inclined free-surface with slope $m\Delta z/\Delta x$, $m \geq 2$ (Figure 3). If we rotate the X–Z coordinate system by the angle $\theta = \tan^{-1}(m\,\Delta z/\Delta x)$ counterclockwise to the X'–Z' system, then in light of equations [2a,b] we have

$$\frac{\partial U'}{\partial z'} + \frac{\partial W'}{\partial x'} = 0 \qquad\qquad\qquad \text{[A-1a]}$$

and

$$\frac{\partial W'}{\partial z'} + (1-2\frac{\beta^2}{\alpha^2})\frac{\partial U'}{\partial x'} = 0 \; . \qquad\qquad \text{[A-1b]}$$

where U', W' are the displacement in X', Z' direction respectively. These two equations will be used to solve for the displacement at every grid point on the free-surface topography with different θ.

Let point 0 be the projection of <i,k> on the line joining points <i+1,k> and <i,k+m>. With first-order accuracy, the displacements at 0 can be approximated by the following linear interpolations:

$$U_0 = \varepsilon_0 U_{i+1,k} + (1 - \varepsilon_0)U_{i,k+m}$$

and

$$W_0 = \varepsilon_0 W_{i+1,k} + (1 - \varepsilon_0)W_{i,k+m} \; ,$$

where

$$\varepsilon_0 = \sin^2\theta \; .$$

Rotate the displacements at the three atoms 0, <i+1,k-1>, and <i,k+m-1> to the inclined system X'–Z' and substitute them into equations [A-1]. We have the following extrapolation formulae:

$$U'_{i,k} = U'_0 - \cos\theta\sin\theta(W'_{i+1,k-1}-W'_{i,k+m-1}) \qquad\qquad \text{[A-2a]}$$

and

$$W'_{i,k} = W'_0 - \cos\theta\sin\theta(1-2\frac{\beta^2}{\alpha^2})(U'_{i+1,k-1}-U'_{i,k+m-1}) \; . \qquad \text{[A-2b]}$$

$U'_{i,k}$ and $W'_{i,k}$ are then rotated back to the original X–Z system by the angle $-\theta$.

9
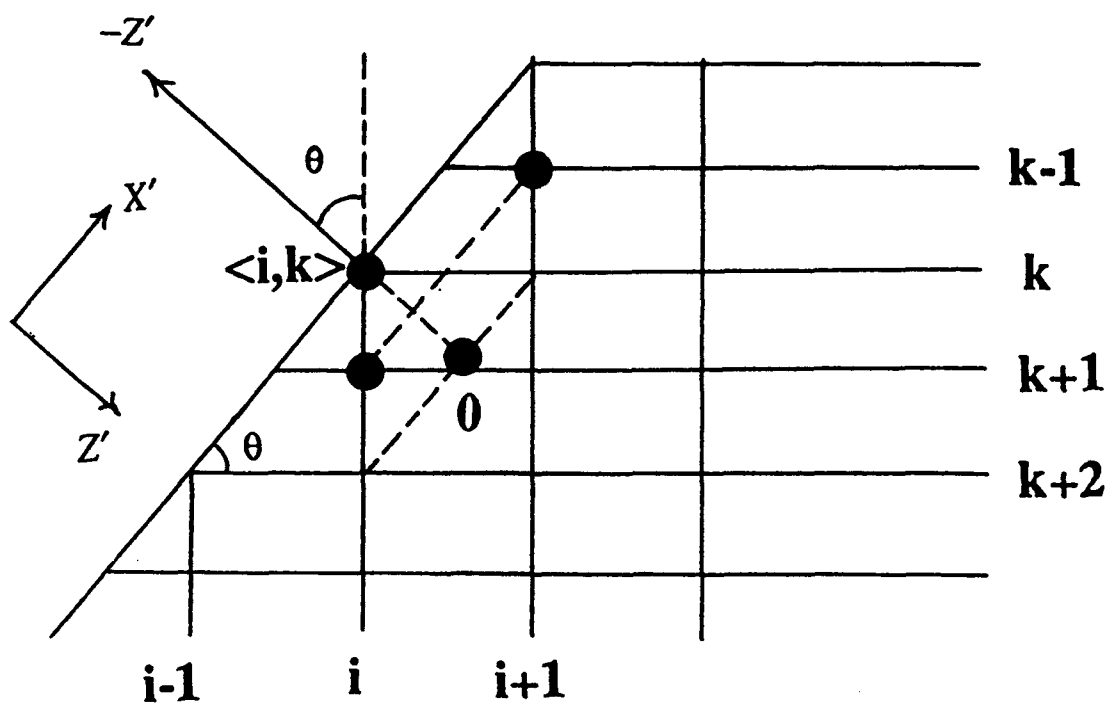
Figure 3

(B) Constant Gentle Slope

For grid point $\langle i,k \rangle$ on an inclined free-surface with slope $\Delta z/\Delta x$ (Figure 4), let

$$\theta = \tan^{-1}(\Delta z/\Delta x)$$

and

$$\epsilon_0 = \sin^2\theta .$$

Let point 0 be the projection of $\langle i,k \rangle$ on the line joining points $\langle i+1,k \rangle$ and $\langle i,k+1 \rangle$. Again, the displacements at 0 can be approximated via

$$U_0 = \epsilon_0 U_{i+1,k} + (1 - \epsilon_0)U_{i,k+1}$$

and

$$W_0 = \epsilon_0 W_{i+1,k} + (1 - \epsilon_0)W_{i,k+1} .$$

Now in the $X'-Z'$ coordinate system, displacements $U'_{i,k}$, $W'_{i,k}$ can be solved via equations [B-1] as

$$U'_{i,k} = U'_0 - \sin\theta\cos\theta(W'_{i+1,k} - W'_{i,k+1}) \qquad \text{[B-1a]}$$

and

$$W'_{i,k} = W'_0 - \sin\theta\cos\theta(1 - 2\frac{\beta^2}{\alpha^2})(U'_{i+1,k} - U'_{i,k+1}) . \qquad \text{[B-1b]}$$

We then rotate $U'_{i,k}$, $W'_{i,k}$ back to the original $X-Z$ system with the angle $-\theta$. Note that this algorithm is simpler than Ilan's (1977) formulation, and the weighting factor $\sin\theta\cos\theta$ in formulae [B-1] is applicable whether $\theta \leq 45°$ or not, although in most actual applications, θ is rarely larger than 45°. Also note that we use gentle and steep in algorithms A and B simply to distinguish whether m, the elevation rising from grid column i to column i+1 in terms of Δz, is equal to one or greater than one.
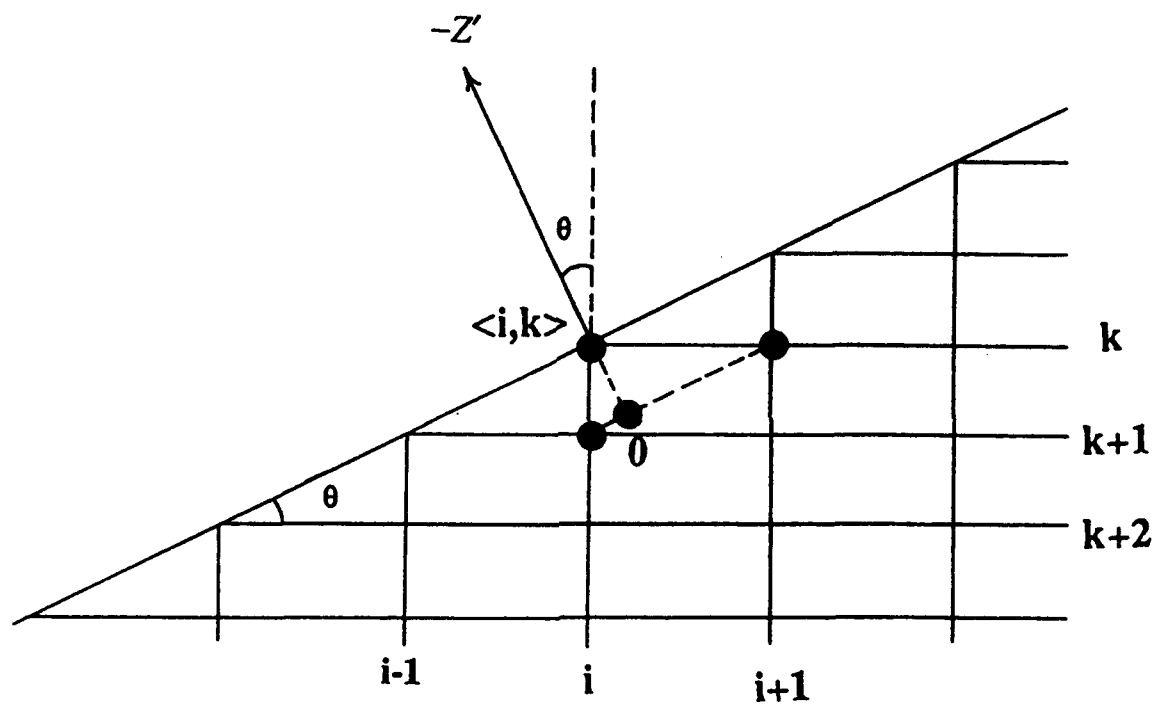
Figure 4

(C) Concave Horizontal-to-gentle Slope Transition

For grid points at the bottom of a canyon with slope $m\Delta z/\Delta x$, $m \geq 1$ (Figure 5), assuming that $\Delta x \geq \Delta z$, let $\theta = \tan^{-1}(m\Delta z/\Delta x)$, $\varepsilon_0 = \tan(\theta/2)\Delta z/\Delta x$, $\varepsilon_1 = \tan(\theta/2)\cot\theta$, and

$$U_0 = (1-\varepsilon_0)U_{i,k+1} + \varepsilon_0 U_{i+1,k+1} , \qquad \text{[C-1a]}$$

$$W_0 = (1-\varepsilon_0)W_{i,k+1} + \varepsilon_0 W_{i+1,k+1} , \qquad \text{[C-1b]}$$

$$U_1 = (1-\varepsilon_1)U_{i-1,k} + \varepsilon_1 U_{i-1,k+m} , \qquad \text{[C-1c]}$$

$$W_1 = (1-\varepsilon_1)W_{i-1,k} + \varepsilon_1 W_{i-1,k+m} , \qquad \text{[C-1d]}$$

$$U_2 = (1-\varepsilon_1)U_{i+1,k} + \varepsilon_1 U_{i+1,k-m} , \qquad \text{[C-1e]}$$

and

$$W_2 = (1-\varepsilon_1)W_{i+1,k} + \varepsilon_1 W_{i+1,k-m} . \qquad \text{[C-1f]}$$

Then,

$$U'_{i,k} = U'_0 - \frac{\Delta z}{2\Delta x}(W'_2 - W'_1) \qquad \text{[C-2a]}$$

and

$$W'_{i,k} = W'_0 - \frac{\Delta z}{2\Delta x}(1 - 2\frac{\beta^2}{\alpha^2})(U'_2 - U'_1) . \qquad \text{[C-2b]}$$

Note that we rotate U, W by the angle $\theta/2$ instead of θ to get U', W' so that the Z' axis is consistent with the direction of the local bisector at grid point $<i,k>$.

For the case $\Delta x < \Delta z$, substitute $\varepsilon_0 = \cot(\theta/2)\Delta x/\Delta z$ and $\varepsilon_1 = \tan\theta \tan(\theta/2)$ in formulae [C-1], and replace $\Delta z/2\Delta x$ in equations [C-2] by $\cot(\theta/2)/2$.
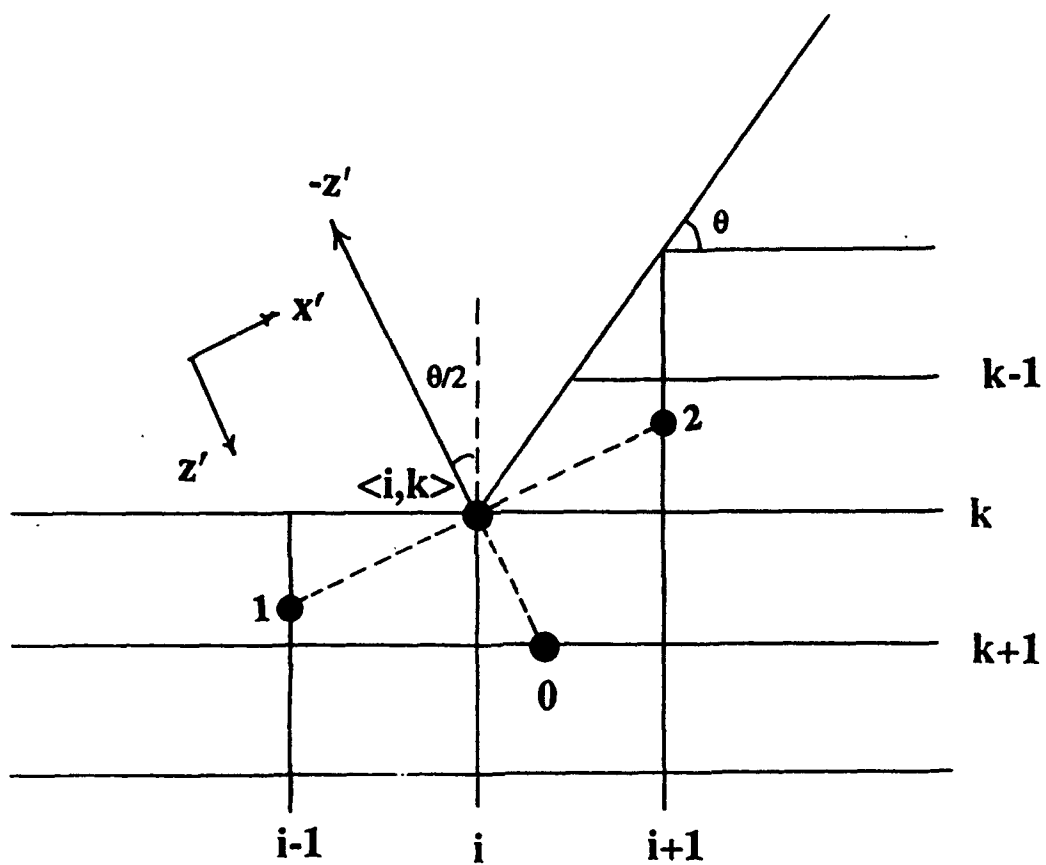
Figure 5

(D) Concave Gentle-to-steep Slope Transition

For grid points with left slope $n\Delta z/\Delta x$ and right slope $m\Delta z/\Delta x$, $m > n$, assuming that $\Delta x \leq n\Delta z$, let $\theta = \tan^{-1}(n\Delta z/\Delta x)$, $\phi = \tan^{-1}(m\Delta z/\Delta x)$, $\eta = (\theta + \phi)/2$, $\varepsilon_0 = \varepsilon_1 = \tan\theta\cot\eta$, $\varepsilon_2 = \tan\eta \cot\phi$, and

$$U_0 = (1-\varepsilon_0)U_{i+1,k} + \varepsilon_0 U_{i+1,k+n} , \qquad \text{[D-1a]}$$

$$W_0 = (1-\varepsilon_0)W_{i+1,k} + \varepsilon_0 W_{i+1,k+n} , \qquad \text{[D-1b]}$$

$$U_1 = (1-\varepsilon_1)U_{i,k+n} + \varepsilon_1 U_{i-1,k+n} , \qquad \text{[D-1c]}$$

$$W_1 = (1-\varepsilon_1)W_{i-1,k+n} + \varepsilon_1 W_{i-1,k+n} , \qquad \text{[D-1d]}$$

$$U_2 = (1-\varepsilon_1)U_{i+1,k} + \varepsilon_1 U_{i+1,k-m} , \qquad \text{[D-1e]}$$

and

$$W_2 = (1-\varepsilon_1)W_{i+1,k} + \varepsilon_1 W_{i+1,k-m} . \qquad \text{[D-1f]}$$

Then,

$$U'_{i,k} = U'_0 - \frac{1}{\tan\eta + \tan\theta}(W'_2 - W'_1) \qquad \text{[D-2a]}$$

and

$$W'_{i,k} = W'_0 - \frac{1}{\tan\eta + \tan\theta}(1 - 2\frac{\beta^2}{\alpha^2})(U'_2 - U'_1) . \qquad \text{[D-2b]}$$

Note that we rotate U, W by angle η to get U', W' so that the Z' axis is consistent with the direction of the local bisector at the grid point $<i,k>$.

For the case that $\Delta x > n\Delta z$ (Figure 6), substitute $\varepsilon_0 = \tan\theta\tan\eta$, $\varepsilon_1 = \tan\theta\cot\eta$, and $\varepsilon_2 = \tan\eta\cot\phi$, in formulae [D-1], and replace $\tan\eta + \tan\theta$ in [D-2] by $\cot\eta + \cot\theta$. Also, replace [D-1a,b] with

$$U_0 = (1-\varepsilon_0)U_{i,k+n} + \varepsilon_0 U_{i+1,k+n} , \qquad \text{[D-3a]}$$

$$W_0 = (1-\varepsilon_0)W_{i,k+n} + \varepsilon_0 W_{i+1,k+n} . \qquad \text{[D-3b]}$$
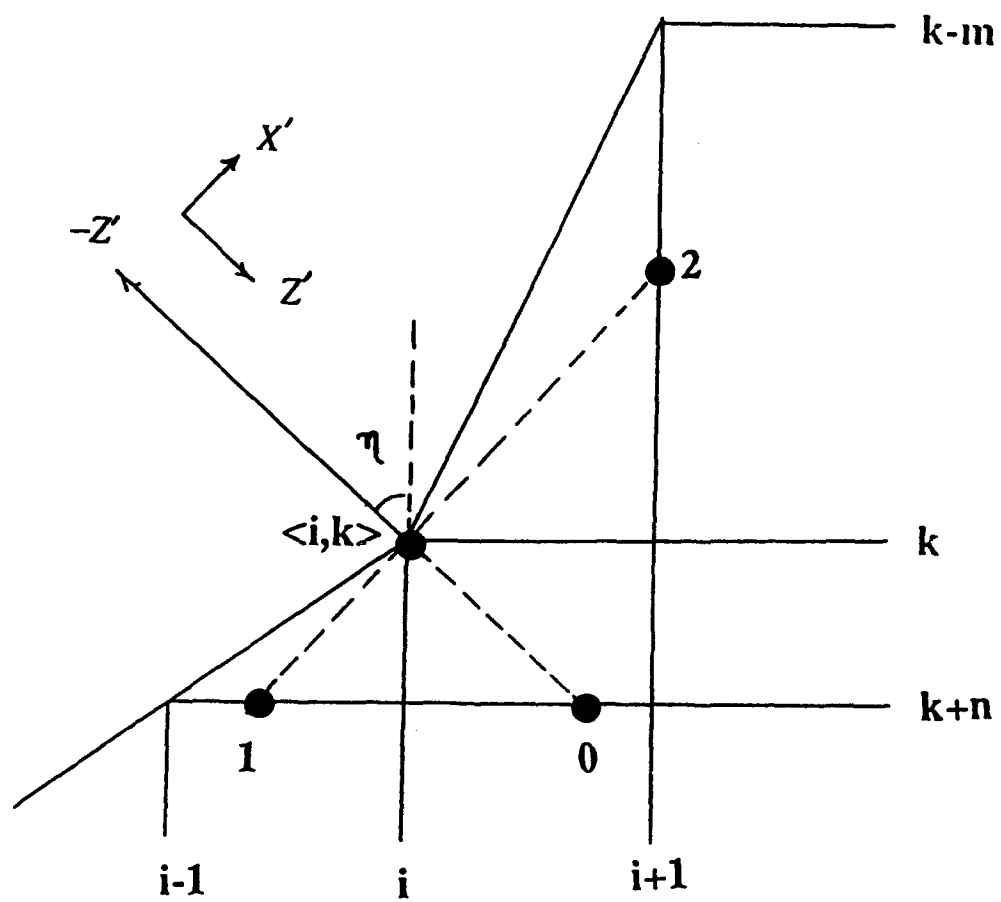
Figure 6

(E) Convex Change In Slope

For grid points with decrease in slope from $n\Delta z/\Delta x$ to $m\Delta z/\Delta x$, $n > m$, let $\theta = \tan^{-1}(n\Delta z/\Delta x)$, $\phi = \tan^{-1}(m\Delta z/\Delta x)$, $\eta = (\theta + \phi)/2$, and $\varepsilon_0 = \tan\eta\Delta z/\Delta x$. If ε_0 is less than 1, then let

$$U_0 = (1-\varepsilon_0)U_{i,k+1} + \varepsilon_0 U_{i+1,k+1} \qquad \text{[E-1a]}$$

and

$$W_0 = (1-\varepsilon_0)W_{i,k+1} + \varepsilon_0 W_{i+1,k+1} , \qquad \text{[E-1b]}$$

as shown in Figure 7b where atom 0 lies between $<i,k+1>$ and $<i+1,k+1>$. Otherwise let $\varepsilon_3 = 1/\varepsilon_0$, and

$$U_0 = (1-\varepsilon_3)U_{i+1,k+1} + \varepsilon_3 U_{i+1,k} \qquad \text{[E-1c]}$$

and

$$W_0 = (1-\varepsilon_3)W_{i+1,k+1} + \varepsilon_3 W_{i+1,k} , \qquad \text{[E-1d]}$$

so that atom 0 lies between $<i+1,k+1>$ and $<i+1,k>$ (Figure 7a).

Now depending on the value of m, we have 2 cases :

(E.1) $m = 1$. Let $<i+1,k>$ be an atom (Figure 7a). Then the diagonal of the molecule passing through $<i+1,k>$ will intersect the ith grid column somewhere between $<i,k>$ and $<i,k+n>$. Let the intersection point be atom 1 (Figure 7a). Note that $\tan\phi < \tan\eta < \tan\theta$, hence, $\varepsilon_1 = (\tan\eta\cot\phi - 1)/(n-1)$ is always between 0 and 1. The displacement at atom 1 can be interpolated as

$$U_1 = (1-\varepsilon_1)U_{i,k+1} + \varepsilon_1 U_{i,k+n} \qquad \text{[E-2a]}$$

and

$$W_1 = (1-\varepsilon_1)W_{i,k+1} + \varepsilon_1 W_{i,k+n} . \qquad \text{[E-2b]}$$

Note that we use point $<i,k+1>$ rather than $<i,k>$ in equations (E-2), since the displacement at $<i,k>$ is unknown. Then,

$$U'_{i,k} = U'_0 - \varepsilon_2(W'_{i+1,k} - W'_1) \qquad \text{[E-3a]}$$

and

$$W'_{i,k} = W'_0 - \varepsilon_2(1 - 2\frac{\beta^2}{\alpha^2}) \cdot (U'_{i+1,k} - U'_1) , \qquad \text{[E-3b]}$$

where $\varepsilon_2 = \tan\phi$ if $\varepsilon_0 \leq 1$, or $\cot\eta$ if $\varepsilon_0 > 1$.

(E.2) $m > 1$. Let atom 2 be at node $<i,k+1>$ (Figure 7b), and $\varepsilon_1 = (2\Delta z\cot\eta/\Delta x)$, so ε_1 is always between 0 and 1.

$$U_1 = (1-\varepsilon_1)U_{i,k-1} + \varepsilon_1 U_{i+1,k-1} \qquad \text{[E-2c]}$$

and

$$W_1 = (1-\varepsilon_1)W_{i,k-1} + \varepsilon_1 W_{i+1,k-1} . \qquad \text{[E-2d]}$$

17

The displacements at point <i,k-1> are computed by extrapolation (see algorithm (G)) since it's outside the grid. Now,

$$U'_{i,k} = U'_0 - \varepsilon_2(W'_1 - W'_{i,k+1}) \qquad \text{[E-3c]}$$

and

$$W'_{i,k} = W'_0 - \varepsilon_2(1 - 2\frac{\beta^2}{\alpha^2})(U'_1 - U'_{i,k+1}) , \qquad \text{[E-3d]}$$

where $\varepsilon_2 = 0.5\tan\eta$ if $\varepsilon_0 \leq 1$, or $\varepsilon_2 = \Delta x/(2\Delta z)$ if $\varepsilon_0 > 1$.

Note that again we rotate U, W by angle η to get U', W' , so that the Z' axis is consistent with the direction of the local bisector at the grid point <i,k>.
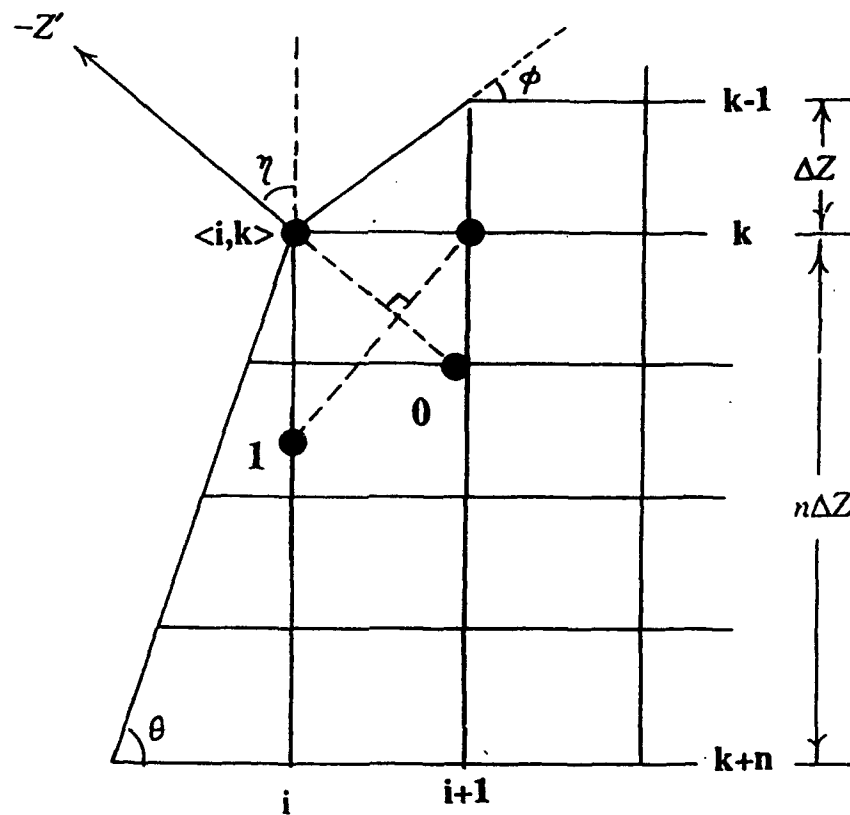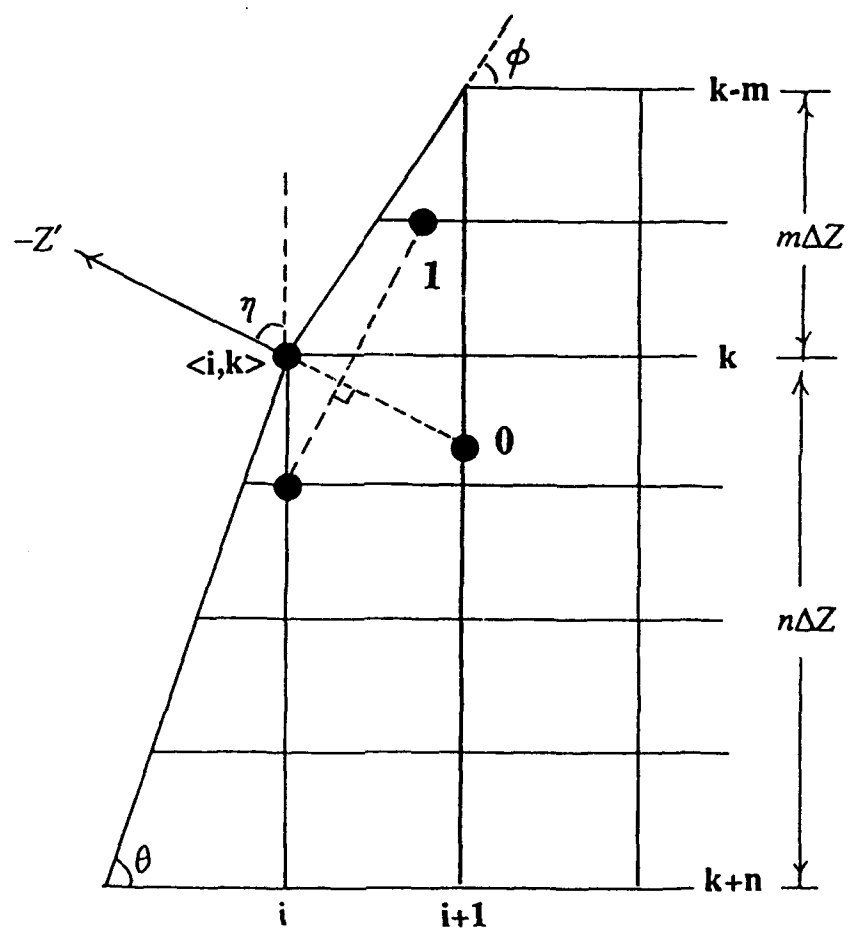
Figure 7

(F) Convex Gentle Slope-to-horizontal Transition

Without loss of generality, we may assume that the topography changes slope from $\Delta z/\Delta x$ to 0 at the crests (Figure 8). Let $\phi = \tan^{-1}(\Delta z/\Delta x)$, $\varepsilon_0 = \tan(\phi/2)\tan\phi$, and $\varepsilon_1 = \tan(\phi/2)\cot\phi$. In this case the offset between the Z-direction and the Z'-direction is $\phi/2$. Let the intersection of the local normal with the (k+1)-th grid row be atom 0. The other two atoms are chosen so that they are collinear with node $<i,k+1>$. Note that $\varepsilon_0 \le 1$ provided $\Delta z \le \sqrt{3}\,\Delta x$, i.e., $\phi \le 60°$. Let

$$U_0 = (1-\varepsilon_0)U_{i,k+1} + \varepsilon_0 U_{i+1,k+1} ,$$ [F-1a]

$$W_0 = (1-\varepsilon_0)W_{i,k+1} + \varepsilon_0 W_{i+1,k+1} ,$$ [F-1b]

$$U_1 = (1-\varepsilon_1)U_{i-1,k+1} + \varepsilon_1 U_{i-1,k+2} ,$$ [F-1c]

$$W_1 = (1-\varepsilon_1)W_{i-1,k+1} + \varepsilon_1 W_{i-1,k+2} ,$$ [F-1d]

$$U_2 = (1-\varepsilon_1)U_{i+1,k+1} + \varepsilon_1 U_{i+1,k} ,$$ [F-1e]

and

$$W_2 = (1-\varepsilon_1)W_{i+1,k+1} + \varepsilon_1 W_{i+1,k} .$$ [F-1f]

Then,

$$U'_{i,k} = U'_0 - \frac{\tan\phi}{2}(W'_2 - W'_1)$$ [F-2a]

and

$$W'_{i,k} = W'_0 - \frac{\tan\phi}{2}(1 - 2\frac{\beta^2}{\alpha^2})(U'_2 - U'_1) .$$ [F-2b]

Here we rotate U, W by angle $\phi/2$ to get U', W' so that the Z' axis is again consistent with the direction of the local bisector at the grid point $<i,k>$.

20
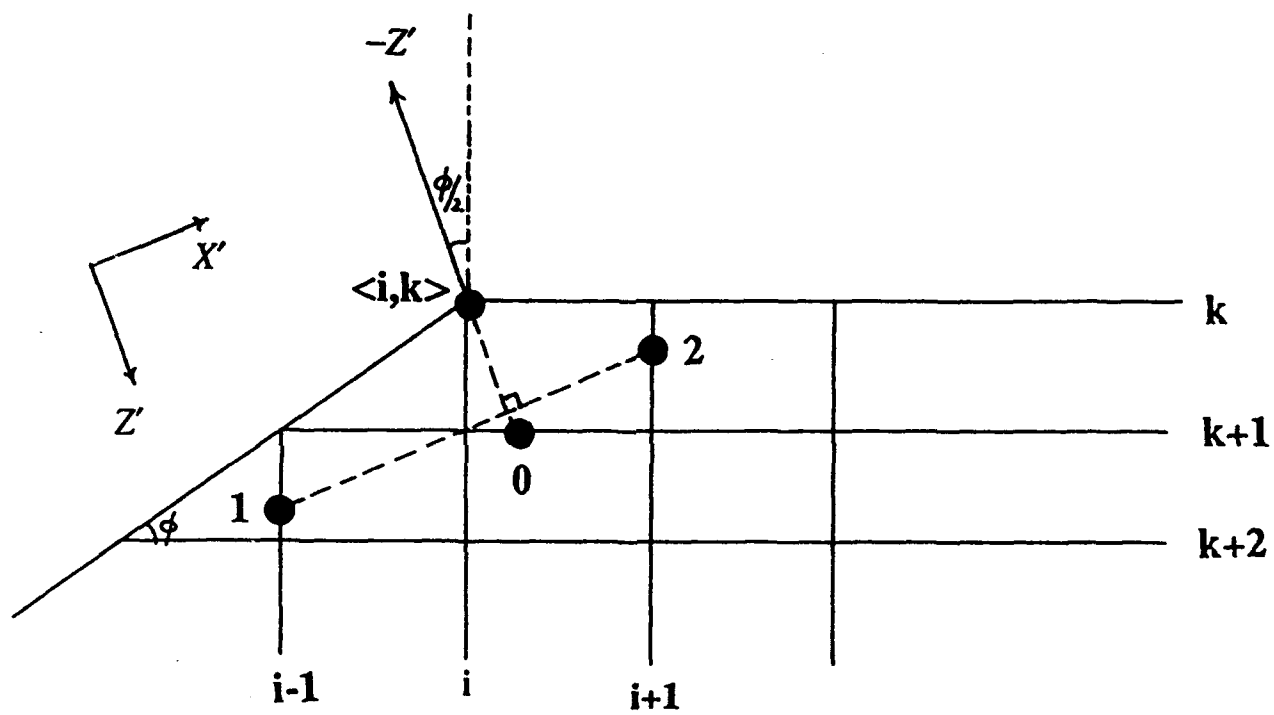
Figure 8

(G) Fictitious Boundary Points for Steep Slope

Suppose that a grid point $<i,k>$ lies on the free-surface with slope $m\Delta z/\Delta x$, $m \geq 1$. Due to the explicit scheme (Equations [1c] and [1d]) we adopt for the interior points, the calculation of the displacements at inner points $<i+1,k>$, $<i+1,k-1>$,....,$<i+1,k-m+1>$ requires displacement values at $<i,k-1>$, $<i,k-2>$,...$<i,k-m>$ which are outside the topography. This difficulty can be easily removed by evaluating m fictitious layers above the topography as follows (Figure 9):

For $1 \leq n \leq m$, let $\varepsilon_0 = (n/m)\sin^2\theta$, where $\theta = \tan^{-1}m\Delta z/\Delta x$, use $U_0 = \varepsilon_0 U_{i+1,k-m} + (1-\varepsilon_0)U_{i,k}$ and $W_0 = \varepsilon_0 W_{i+1,k-m} + (1-\varepsilon_0)W_{i,k}$ as the approximate displacement of the orthogonal projection of point $<i,k-m+n>$ on the free-surface.

Now rotate displacements at points $<i+1,k-m>$, $<i,k>$ and 0 by angle θ as before to extrapolate the approximate motion at point $<i,k-m+n>$:

$$U'_{i,k-m+n} = U'_0 - \frac{n}{m}\sin\theta\cos\theta(W'_{i+1,k-m} - W'_{i,k})$$

and

$$W'_{i,k-m+n} = W'_0 - (1-2\frac{\beta^2}{\alpha^2})\frac{n}{m}\sin\theta\cos\theta(U'_{i+1,k-m} - U'_{i,k}) .$$

Then rotate U', W' back to the original system.

Figure 9

2.4 Some Remarks on Topographic Algorithms

Even in the simplest half-space models, the central-difference approximation (formulae 2c,d) and the one-sided approximation (formulae 2e,f) of the boundary conditions are only conditionally stable. When quarter planes are involved, the range of stability is inevitably smaller. Since our schemes are a (rotated) extension of these two methods and since we are dealing with more complicated irregular geometries, a stronger limitation of Poisson's ratios should apply. It is obvious that our scheme has truncation error of order one (with respect to the mesh spacings) due to the spatial discretization and linear interpolation, as well as the local asymmetry in our formulation, even though the original (*i.e.*, unrotated) central-difference approximation (2c,d) has second-order accuracy. Nevertheless, better accuracy can be achieved by sampling the polygon with a finer grid at the expense of computation. All algorithms are of the explicit type, since only interior nodes nearby are needed for evaluating tangential derivatives. The actual surface configuration implied by this scheme is a somewhat smoothed version of the original discretized polygonal boundary.

Recently a number of techniques have been pursued in an effort to improve the computational performance of finite-difference solutions to wave equations. These include higher-order schemes, implicit rather than explicit methods, velocity-stress schemes, *etc.*. Our formulations were developed mainly to adapt to the traditional explicit second-order finite-difference schemes for wave equation (equations 1) as described by Alterman, Boore, and Kelly because of its popularity. Incorporation of similar treatments of a free boundary with elastodynamic equations might be promising, since a velocity-stress scheme (*e.g.*, Virieux, 1986) is more tractable than the standard displacement schemes at liquid-solid interfaces.

Alternative approaches are available to handle seismological problems involving topographic structures. For instance, the finite-element method offers another natural solution with which one can use more general grid elements such as triangles or even higher order forms instead of the rectangular grids used in the finite-difference method. Drake (1972) and Ohtsuki *et al.* (1984) use the steady-state finite-element method and the transient finite-element method respectively to study the scattering of Rayleigh waves by topography. Finite-difference and finite-element methods can be interpreted as degenerate cases of each other under some conditions (Lapidus and Pinder, 1982). It is reported that finite-element methods give superior accuracy relative to finite-difference methods when modeling elastic media with Poisson's ratio between 0.3 and 0.45, and the accuracy is comparable to finite-difference methods for media with Poisson's ratio less than 0.3 (Marfurt, 1984). The major advantage of the finite-difference method over finite-element methods is its simplicity in implementation. Our work shows how the finite-difference technique can be extended to an irregular free-surface with special treatments.

3. SAMPLE INPUT FILES FOR FD2

"Fd2" reads in control parameters through the standard input and dumps the error messages to the standard output. The output synthetics as well as the snapshots of the wavefield are stored in separate output buffers. The source medium file is specified in the input file or assumed to be a preset homogeneous half space. Topography can be specified as an input file. A sample input file is shown here with each line of argument discussed in more detail at the end. For the user's convenience, an interactive routine "fd_menu" is available which would create the input parameter file.

Sample Input Parameter File

```
[1] grid dimension kw,kh
800 600
[2] x,z spacings of the grid mesh & temporal spacing: dx,dz,dt
0.25 0.25 0.025
[3] homogeneous (0), heterogeneous (1,2)
2
inVp
inVs
inRho
[4] topography file
none
[5] choose wave type
3
[6] incident angle, i0,j0, wvlns
20.00 400 32 5.0
[7] option for snapshot display: component,AGC,begin & end column
"B" 1
   1  800    1 8001 32 200
 401  800    1 8001 32 100
 201   00    1 5001  2 600
 301   00  801 2000  2 250
 701   00  901 1261  2 100
 901   00 1201 1561  2 100
1101   00 1381 1801  2 100
1301   00 1681 2161  2 100
1501   00 1941 2341  2 100
[8] # of seismographs
10
[9] coordinates of sensors: (2 lines, line 1=X's, line 2=Z's)
1 200 400 600 800 -1 -200 -400 -600 -800
2  2  2  2  2 3  3  3  3  3
[10] total # of iterations; # of iterations/snapshot
8001 200
[11] marching grid (>0==>yes)? total grid width desired:
400 1200
```

Remarks:

Item (1)

The grid size specifies the number of nodes in the horizontal and vertical directions. The program will stop if the requested grid size exceeds the predefined size, which is currently compiled with

25

800 by 600 nodes on CSS' SUN4.

Item (2)

The grid mesh, ΔX and ΔZ, is measured in km. The temporal spacing is in sec. Once the grid mesh is specified, the temporal spacing should be determined so that the stability can be ensured throughout the iterations.

Item (3)

If 0, the default homogeneous model with density, ρ, of 2.5gm/cc, and $\lambda = \mu = 21$ for the soil, which implies $V_P = 5.02$km/s and $V_S = 2.9$km/s.

If 1, the program expects to read in λ, μ, and ρ fields.

If 2, the program expects to read in V_P, V_S, and ρ fields.

Item (5)

The initial wave could be

(+1) broadband planar P wave of Ohnaka shape,

(-1) broadband planar S wave of Ohnaka shape,

(+2) monochromatic planar P wave of sinusoidal shape,

(-2) monochromatic planar S wave of sinusoidal shape,

(+3) pure compressional wave generated at a single point,

(-3) double-couple point source,

(+4) fundamental mode Rayleigh wave with Ricker wavelet shape,

(+5) a (time-series) P driver file shaking a single point,

(+6) arbitrary wavefield setting,

(+7) broadband planar P wave of Gaussian shape,

(-7) broadband planar S wave of Gaussian shape,

(+8) ripple-fired explosions with multiple sources of type (+3),

(+9) ripple-fired explosions with multiple sources of type (+5).

Except for cases (+5) and (+9) in which the shaker or driver file must be generated elsewhere in advance, "fd2" is completely self-contained to initialize the wavefields at 2 consecutive time instants to produce proper wave propagation.

Item (6)

(a) the wave length (in km) is needed for a point source, sine or Rayleigh wave

(b) the location of the source point can also be used to adjust boundary conditions

Absorbing boundary condition is default for the bottom and side edges. For normally incident planar waves (options 1, 2, 7), the side edges would be symmetric. Free surface is assumed on the top of the grid whenever a nontrivial topography is involved. All these boundary conditions can be altered by choosing appropriate input parameters. For instance, in the case of point source (options 3, 5, 8, 9) *without* topography, there are 3 more options available by playing with incident angle:

(1) *0-degree indicates that all 4 edges are symmetric,*

(2) *360-degree indicates that all 4 edges are absorbing,*

(3) *720-degree indicates that a symmetric top with absorbing sides and bottom.*

These options are meant only to demonstrate the effects of miscellaneous boundary conditions. In reality, models with free-surface boundary condition on the top and the absorbing boundary

26

condition at the remaining three edges would be the most useful ones. In this sample input file, the incident angle of 20° has no effect and hence the default boundary condition for source option +3 will be used, which is absorbing side.

Item (7)

Program *"fd2"* converts the numerical wavefields into the character wavefields and stores these snapshots in ASCII text files. The output wavefield could be the whole grid or only a portion of the grid as specified in the input parameter file. An input parameter determines whether fixed gain or automatically adjustable scale is used in the conversion procedure. Displacements and/or strain may be recorded as a time series at any interior points for the strain or any grid points for the displacements.

7 options for snapshot displaying are available:

        H : horizontal wave fields

        V : vertical wave fields

        B : both horizontal & vertical wve fields

        S : dilatational & rotational strain fields

        M : combined displacement fields

        A : all components will be shown

AGC > 0 => resolution adjusted for each frame individually,

At most 9 slices (stripes) can be saved in compressed files with prefix "S1" through "S9", respectively. Each stripe needs one line to specify (1) beginning column, (2) ending column, (3) beginning time, (4) ending time, (5) beginning row, and (6) ending row. If any of the three ending entity is smaller than its associated beginning entity, then that stripe will not be shown at all. In this example, only two stripes are stored in compress ASCII files. Files S1* store the upper 200 rows of the whole wavefield (800-grid wide) at a rate of one snapshot per 200 iterations (*cf.* item [10]) throughout the 8001 iterations (*cf.* item [10]). Files S2*, however, store the central portion of the grid from column 401 to column 800. Also, only the top 100 rows will be shown, as specified in the input file. The remaining seven stripes all have an ending column (00 in this case) smaller than the beginning column, which simply turns off their snapshot output. All snapshots are shown from row 2 and down. However, a different "beginning" row can be given to force the gray level be normalized by the peak displacement of a subgrid. In this example, the gray scale is determined by 32th row and below, although the top portion will be shown as well.

Item (9)

(a) list X-coordinates of all sensors first

(b) negative X-coordinate means strain sensor

(c) it should be consistent with the number of sensors as specified in Item (8)

Item (10)

There will be 8001 iterations in total in this example, and one snapshot will be produced for every 200 iterations.

Item (11)

If a number larger than 0 is given, the marching-grid feature will be turned on, and the grid will be shifted by that number of columns when the wavefront is approaching the right edge. In this example, 400 columns will be shifted each time. The total grid width desired is 1200, which is the

original grid size, 800, plus 400 columns, so only one shifting will be performed (*cf.* Step 4 of Example 3).

Sample Topography File

The following sample file defines a simple ramp:

```
10
00 00 00 00 00 00 01 02 03 04 05 06 07 08 08 08 08 08 08 08 08 08 08 08 08
```

The 1st line gives the "reference floor" level of the topography. The 2nd line gives the elevation with respect to the reference level. For example, the "03" in line 2 actually means the 7th (=10-3) row from the top of the grid. Note that the reference level itself must be deep enough so that the peak of the topography is still within the grid. Each segment must contain at least 2 sub-segments before the slope changes.

Sample Input File of Velocity Model

```
grid size:   20   25
grid spacing:    0.1000    0.1000
Self-Similar Medium
Extracted from another model
5 (dummy line)
6 (dummy line)
7 (dummy line)
8 (dummy line)
    0.4927E+01  0.4962E+01  0.5106E+01  0.5123E+01  0.5128E+01
    0.5078E+01  0.5213E+01  0.5393E+01  0.5229E+01  0.5239E+01
    0.5584E+01  0.5685E+01  0.5583E+01  0.5542E+01  0.5256E+01
    .........
```

Lines 1 and 2 specify the grid size and and the grid spacing. Lines 3 and 4 are for identification purpose. Lines 5 through 8 are dummies. The remaining lines give P-wave velocity (or S-wave velocity, or density) at the node (i,j) where i=1,...,kw; j=1,...,kh. Lines 1 and 2 are read with fixed format of (i10x, 2i5) and (13x, 2f10.4), respectively.

28

4. OUTPUT FILES GENERATED BY FD2

A number of different output formats are commonly used in finite-difference calculations. In fact, one of the advantages of the finite-difference method is the ability to save particle displacements for any number of points on the grid and for all times. The synthetics are nothing but the time history recorded at specific grid points, for example. A particularly informative way to visualize wave propagation through the models is by using numerical Schlieren diagrams. These "snapshots" of the wavefield traveling through the grid are generated by saving the displacement at each grid point for a given time step.

In our implementation, the program converts numerical wavefields into character wavefields and stores these snapshots in ASCII text files. It consumes relatively small storage space, as each grid point only needs one byte. The output wavefield could be the whole grid or only certain portion of the grid. An input parameter determines whether a fixed gain or an automatically adjustable scale is used in the conversion procedure.

Displacements and/or strain may be recorded as a time series at any interior points for the strain or any grid points for the displacements.

Program also stores the wavefields at two consecutive instants and all required parameters at a prespecified rate so that it can be re-started in case the job is terminated in the middle.

5. EXAMPLE 1: PLANAR WAVE INCIDENT UPON SIMPLE RAMP

The first example demonstrates how to set up an experiment for modeling the propagation of a normally incident plane P wave through a model with a 45° ramp on the top of the grid and von Neumann (*i.e.* 0-slope or symmetric) boundary conditions on both sides. The homogeneous medium has compressional and shear velocities of 5.02 and 2.898 km/s, respectively.

Step 1: Generating Topography File

```
cat << / > inTOP
66
00 00 00 00 00 00 00 00 00 00 00 00 00 00 00 00 00 00 00 00 00 00 00 00 00 00 00 00 00 00 00 00 00
00 00 00 00 00 00 00 00 00 00 00 00 00 00 00 00 00 00 00 00 00 00 00 00 00 00 00 00 00 00 00 00 00
00 00 00 00 00 00 00 00 00 00 00 00 00 00 00 00 00 00 00 00 00 00 00 00 00 00 00 00 00 00 00 00 00
00 00 00 00 00 00 00 00 00 00 00 00 00 00 00 00 00 00 00 00 00 00 00 00 00 00 00 00 00 00 00 00 00
00 00 00 00 00 00 00 00 00 00 00 00 00 00 00 00 00 00 00 00 00 00 00 00 00 00 00 00 00 00 00 00 00
00 00 00 00 00 00 00 00 00 00 00 00 00 00 00 00 00 00 00 00 00 00 00 00 00 00 00 00 00 00 00 00 00
00 00 00 00 00 00 00 00 00 00 00 00 00 00 00 00 00 00 00 00 00 00 00 00 00 00 00 00 00 00 00 00 00
00 00 00 00 00 00 00 00 00 00 01 02 03 04 05 06 07 08 09 10 11 12 13 14 15 16 17 18 19 20
21 22 23 24 25 26 27 28 29 30 31 32 33 34 35 36 37 38 39 40 41 42 43 44 45 46 47 48 49 50
51 52 53 54 55 56 57 58 59 60 61 62 63 64 64 64 64 64 64 64 64 64 64 64 64 64 64 64 64 64 64
64 64 64 64 64 64 64 64 64 64 64 64 64 64 64 64 64 64 64 64 64 64 64 64 64 64 64 64 64 64 64
64 64 64 64 64 64 64 64 64 64 64 64 64 64 64 64 64 64 64 64 64 64 64 64 64 64 64 64 64 64 64
64 64 64 64 64 64 64 64 64 ₤ . 64 64 64 64 64 64 64 64 64 64 64 64 64 64 64 64 64 64 64 64 64
64 64 64 64 64 64 64 64 64 64 64 64 64 64 64 64 64 64 64 64 64 64 64 64 64 64 64 64 64 64 64
64 64 64 64 64 64 64 64 64 64 64 64 64 64 64 64 64 64 64 64 64 64 64 64 64 64 64 64 64 64 64
64 64 64 64 64 64 64 64 64 64 64 64 64 64 64 64 64 64 64 64 64 64 64 64 64 64 64 64 64 64 64
64 64 64 64 64 64 64 64 64 64 64 64 64 64 64 64 64 64 64 64 64 64 64 64 64 64 64 64 64 64 64
64 64 64 64 64 64 64 64 64 64 64 64 64 64 64 64 64 64 64 64 64 64 64 64 64 64 64 64 64 64 64
!
```

Step 2: Running FD

```
#=== generate input parameter file for fd
cat << EOF > inFD
1) grid dimension kw,kh
500 202
2) x,z spacings of the grid mesh & temporal spacing: dx,dz,dt
0.01 0.01 0.001
3) homogeneous (0), heterogeneous (1,2)
0
inVp
inVs
inRho
4) topography file
inTOP
5) choose wave type
7
6) alpha, i0,j0, wvlns
0.00 40 -80 0.2
7) option for snapshot display: component,AGC,begin & end column
"m" 1
```

```
   1  500    1 5001 2 202
 201   00    1 2001 2 120
 201   00    1 5001 2 600
 301   00  801 2000 2 250
 701   00  901 1261 2 100
 901   00 1201 1561 2 100
1101   00 1381 1801 2 100
1301   00 1681 2161 2 100
1501   00 1941 2341 2 100
8) # of seismographs
31
9) coordinates of sensors: (line 1=X's,line 2=Z's,negX=strain sensor)
012 028 044 060 076 092 108 124 140 156 172 188 204 220
236 252 268 284 300 316 332 348 364 380 396 412 428 444 460 476 492
066 066 066 066 066 066 066 066 066 066 066 066 066 066
050 034 018 002 002 002 002 002 002 002 002 002 002 002 002 002 002
10) total # of iterations; # of iteration/snapshot
700 100
11) marching grid (>0==>yes)? total grid width desired:
0 500
EOF

#=== run fd
fd2 < inFD > & FD_msg

#=== demultiplex time series
fdsplt < data.0 > & error
```

31

The fd2 generates the following error message

FD code version 930405, RSJ
Compiled with grid= 800 600
Grid desired= 500 202
Mesh & temporal spacings = .0100 .0100 .0010
Homogeneous model
Input topography file=inTOP
SETTOP> ihh= 66
SETTOP> itpg() read (sampled every 50 columns):
*   0 0 0 0 0 31 64 64 64 64*
SETTOP> idh(l,3) (sampled every 50 columns):
*   66 66 66 66 66 35 2 2 2 2*
Boundary flags (l-r-t-b): 0 0 3 0
(Initial setting as in SETTOP)
grid> jend(column 1)= 65
grid> jend(column lcw)= 1
GRID> geological model ready.
Grid sampled per 51 by 21 nodes
Lambda field
* 2: .0 .0 .0 .0 .0 .0 21.0 21.0 21.0 21.0*
23: .0 .0 .0 .0 .0 .0 21.0 21.0 21.0 21.0
44: .0 .0 .0 .0 .0 21.0 21.0 21.0 21.0 21.0
65: .0 .0 .0 .0 .0 21.0 21.0 21.0 21.0 21.0
86: 21.0 21.0 21.0 21.0 21.0 21.0 21.0 21.0 21.0 21.0
107: 21.0 21.0 21.0 21.0 21.0 21.0 21.0 21.0 21.0 21.0
128: 21.0 21.0 21.0 21.0 21.0 21.0 21.0 21.0 21.0 21.0
149: 21.0 21.0 21.0 21.0 21.0 21.0 21.0 21.0 21.0 21.0
170: 21.0 21.0 21.0 21.0 21.0 21.0 21.0 21.0 21.0 21.0
191: 21.0 21.0 21.0 21.0 21.0 21.0 21.0 21.0 21.0 21.0
Mu field
* 2: .0 .0 .0 .0 .0 .0 21.0 21.0 21.0 21.0*
23: .0 .0 .0 .0 .0 .0 21.0 21.0 21.0 21.0
44: .0 .0 .0 .0 .0 21.0 21.0 21.0 21.0 21.0
65: .0 .0 .0 .0 .0 21.0 21.0 21.0 21.0 21.0
86: 21.0 21.0 21.0 21.0 21.0 21.0 21.0 21.0 21.0 21.0
107: 21.0 21.0 21.0 21.0 21.0 21.0 21.0 21.0 21.0 21.0
128: 21.0 21.0 21.0 21.0 21.0 21.0 21.0 21.0 21.0 21.0
149: 21.0 21.0 21.0 21.0 21.0 21.0 21.0 21.0 21.0 21.0
170: 21.0 21.0 21.0 21.0 21.0 21.0 21.0 21.0 21.0 21.0
191: 21.0 21.0 21.0 21.0 21.0 21.0 21.0 21.0 21.0 21.0
Density field
* 2: .0 .0 .0 .0 .0 .0 2.5 2.5 2.5 2.5*
23: .0 .0 .0 .0 .0 .0 2.5 2.5 2.5 2.5
44: .0 .0 .0 .0 .0 2.5 2.5 2.5 2.5 2.5
65: .0 .0 .0 .0 .0 2.5 2.5 2.5 2.5 2.5
86: 2.5 2.5 2.5 2.5 2.5 2.5 2.5 2.5 2.5 2.5
107: 2.5 2.5 2.5 2.5 2.5 2.5 2.5 2.5 2.5 2.5
128: 2.5 2.5 2.5 2.5 2.5 2.5 2.5 2.5 2.5 2.5
149: 2.5 2.5 2.5 2.5 2.5 2.5 2.5 2.5 2.5 2.5
170: 2.5 2.5 2.5 2.5 2.5 2.5 2.5 2.5 2.5 2.5
191: 2.5 2.5 2.5 2.5 2.5 2.5 2.5 2.5 2.5 2.5
Squared P velocity field

```
  2:   .0   .0   .0   .0   .0   .0  25.2  25.2  25.2  25.2
 23:   .0   .0   .0   .0   .0   .0  25.2  25.2  25.2  25.2
 44:   .0   .0   .0   .0   .0  25.2  25.2  25.2  25.2  25.2
 65:   .0   .0   .0   .0   .0  25.2  25.2  25.2  25.2  25.2
 86:  25.2  25.2  25.2  25.2  25.2  25.2  25.2  25.2  25.2  25.2
107:  25.2  25.2  25.2  25.2  25.2  25.2  25.2  25.2  25.2  25.2
128:  25.2  25.2  25.2  25.2  25.2  25.2  25.2  25.2  25.2  25.2
149:  25.2  25.2  25.2  25.2  25.2  25.2  25.2  25.2  25.2  25.2
170:  25.2  25.2  25.2  25.2  25.2  25.2  25.2  25.2  25.2  25.2
191:  25.2  25.2  25.2  25.2  25.2  25.2  25.2  25.2  25.2  25.2
```
Squared S velocity field
```
  2:   .0   .0   .0   .0   .0   .0   8.4   8.4   8.4   8.4
 23:   .0   .0   .0   .0   .0   .0   8.4   8.4   8.4   8.4
 44:   .0   .0   .0   .0   .0   8.4   8.4   8.4   8.4   8.4
 65:   .0   .0   .0   .0   .0   8.4   8.4   8.4   8.4   8.4
 86:   8.4   8.4   8.4   8.4   8.4   8.4   8.4   8.4   8.4   8.4
107:   8.4   8.4   8.4   8.4   8.4   8.4   8.4   8.4   8.4   8.4
128:   8.4   8.4   8.4   8.4   8.4   8.4   8.4   8.4   8.4   8.4
149:   8.4   8.4   8.4   8.4   8.4   8.4   8.4   8.4   8.4   8.4
170:   8.4   8.4   8.4   8.4   8.4   8.4   8.4   8.4   8.4   8.4
191:   8.4   8.4   8.4   8.4   8.4   8.4   8.4   8.4   8.4   8.4
```
(Vs/Vp)**2
```
  2:   .00   .00   .00   .00   .00   .00   .33   .33   .33   .33
 23:   .00   .00   .00   .00   .00   .00   .33   .33   .33   .33
 44:   .00   .00   .00   .00   .00   .33   .33   .33   .33   .33
 65:   .00   .00   .00   .00   .00   .33   .33   .33   .33   .33
 86:   .33   .33   .33   .33   .33   .33   .33   .33   .33   .33
107:   .33   .33   .33   .33   .33   .33   .33   .33   .33   .33
128:   .33   .33   .33   .33   .33   .33   .33   .33   .33   .33
149:   .33   .33   .33   .33   .33   .33   .33   .33   .33   .33
170:   .33   .33   .33   .33   .33   .33   .33   .33   .33   .33
191:   .33   .33   .33   .33   .33   .33   .33   .33   .33   .33
```
Selected wave type = 7

 0. 40 -80 .200000003

m component will be displayed

AGC flag= 1

Display left, right (column), start, end (dt), top, bottom (row)
```
   1  500     1  5001    2  202
 201    0     1  2001    2  120
 201    0     1  5001    2  202
 301    0   801  2000    2  202
 701    0   901  1261    2  100
 901    0  1201  1561    2  100
1101    0  1381  1801    2  100
1301    0  1681  2161    2  100
1501    0  1941  2341    2  100
```
 31 seismometers
```
 12   28   44   60   76   92  108  124  140  156
172  188  204  220  236  252  268  284  300  316
332  348  364  380  396  412  428  444  460  476
492
 66   66   66   66   66   66   66   66   66   66
 66   66   66   66   50   34   18    2    2    2
```

```
2  2  2  2  2  2  2  2  2  2
2
700 iterations,  100 steps per break
Vector sum of displacements
Display flag=   6
Plane P wave (Ohnaka or Gaussian shape)
body> P velocity near grid bottom=   5.02
body> wavelet span (km)=     .318
body> left wavefront starts roughly at   79 row
body> wavelet has z-length roughly   31 points
Incident Angle:   .00deg
Boundary Flags (l-r-t-b): 1130
(tape 19) data.0 opened!
FARPS interface at depth = kh/2=       101
 Snapshot S1000: now,loop,ksu,jsu,ideps=   1   1   1  500    2  202
 Snapshot S1001: now,loop,ksu,jsu,ideps= 101   1   1  500    2  202
 Seismograms output, loop    101
 Snapshot S1002: now,loop,ksu,jsu,ideps= 201   1   1  500    2  202
 Seismograms output, loop    201
 Snapshot S1003: now,loop,ksu,jsu,ideps= 301   1   1  500    2  202
 Seismograms output, loop    301
 Snapshot S1004: now,loop,ksu,jsu,ideps= 401   1   1  500    2  202
 Seismograms output, loop    401
 Snapshot S1005: now,loop,ksu,jsu,ideps= 501   1   1  500    2  202
 Seismograms output, loop    501
 Snapshot S1006: now,loop,ksu,jsu,ideps= 601   1   1  500    2  202
 Seismograms output, loop    601
 Snapshot S1007: now,loop,ksu,jsu,ideps= 701   1   1  500    2  202
 Seismograms output, loop    701
Seismogram and snapshot files closed
Wavefields backup done at iteration    701
```

Step 3: Generating Snapshots

```
#=== sample script to plot out sna~shots with routine "movie"
set nonomatch

#— prepare label for figures
cat << EOF > Label
45-deg ramp, Guassian planar wave
Grid 500*202, dx=10m, dt=1ms
Half space: Vp=5.02km/s, Vs=2.898km/s
EOF

#— change the label
set kk=( S1000 S1001 S1002 S1003 )
foreach i ( 1 2 3 4 )
ex $kk[$i] << EOF >> Junk
4,6d
3
r Label
1
wq
EOF
end

#— plot out snapshots with "movie"
movie -w -i 3 -m 4 $kk > & Error
```

Figure 10 shows the propagation of a normally incident planar Gaussian P wave through a model with a 45° ramp on the top of the grid and von Neumann (*i.e.* 0-slope or symmetric) boundary conditions on both sides. The homogeneous medium has the compressional and shear velocities of 5.02 and 2.898 km/s, respectively. Shading in each snapshot is proportional to the displacement amplitude $\sqrt{U^2 + W^2}$.

The accuracy of the results was tested empirically by comparing results obtained from two separate finite-difference runs. In the first run, we adopted grid spacings $\Delta x = \Delta z = 0.01$km. In the second run, we used one-half the vertical spacing but doubled the vertical exaggeration at discretization. Thus two algorithms, B and A in Section 2.3, were used separately in these two finite-difference runs. Excellent agreement was obtained, indicating that the two algorithms A and B are consistent and that both solutions are good approximations to the true solutions, by Lax's equivalence theorem (Smith, 1978; Mitchell and Griffiths, 1980). The appropriate P–SV conversions and the reflections and diffractions satisfying Snell's law and Huygen's principle are clearly visible in the successive snapshots taken every 0.1 second, as shown in Figure 10. It is easy to verify the first-order accuracy in spatial increment of our one-sided explicit representation of the free-surface boundary conditions in this case.

FD step 0
SQRT(V**2+H**2) .000SEC, 1 500 1 202
X Tic Mark = 1 Unit; Z Tic Mark = 1 Unit
.00000E+00 .99878E+00

FD step 100
SQRT(V**2+H**2) .100SEC, 1 500 1 202
X Tic Mark = 1 Unit; Z Tic Mark = 1 Unit
.00000E+00 .20062E+01

FD step 200
SQRT(V**2+H**2) .200SEC, 1 500 1 202
X Tic Mark = 1 Unit; Z Tic Mark = 1 Unit
.00000E+00 .12963E+01

FD step 300
SQRT(V**2+H**2) .300SEC, 1 500 1 202
X Tic Mark = 1 Unit; Z Tic Mark = 1 Unit
.00000E+00 .16615E+01
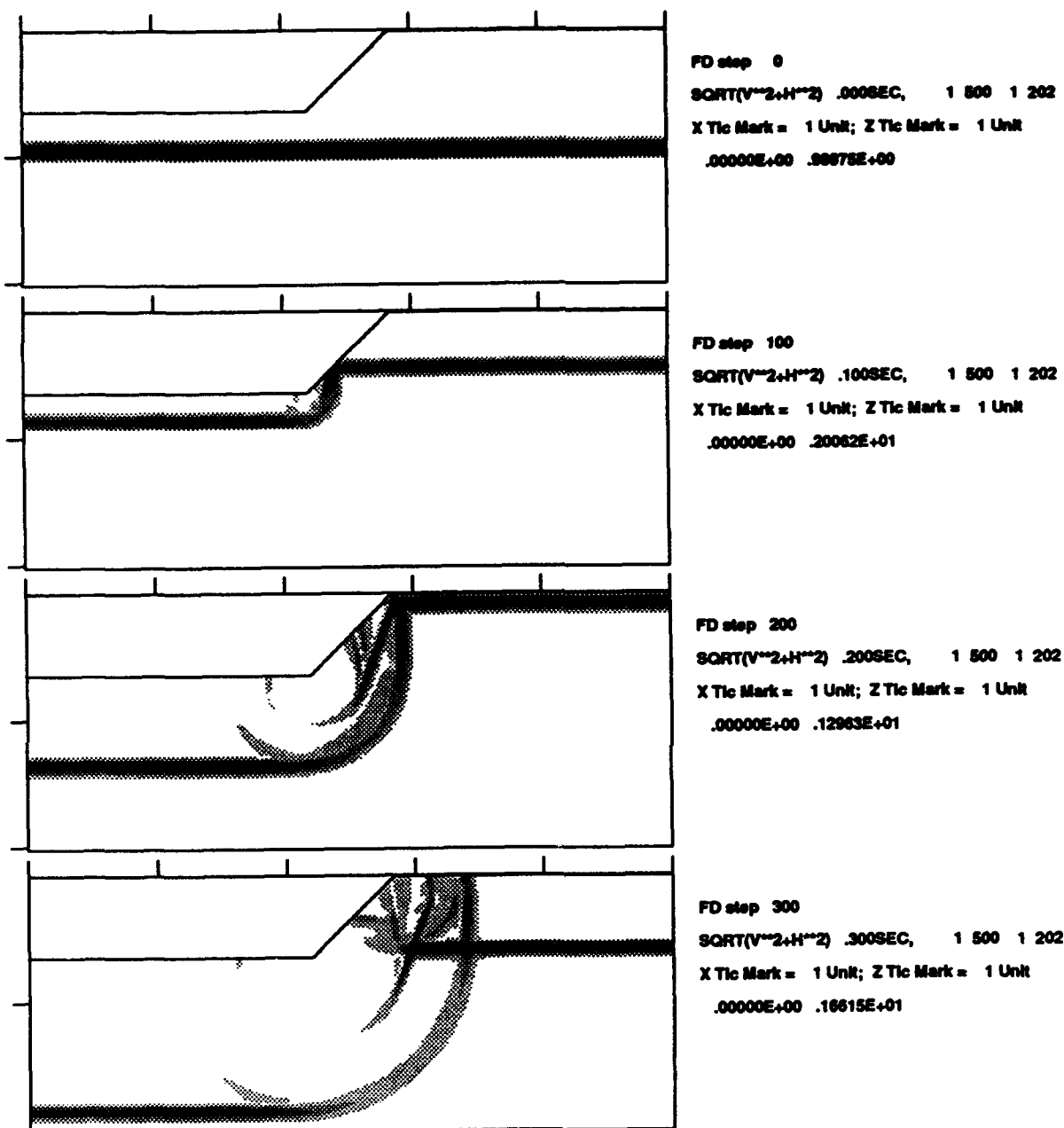
45-deg ramp, Guassian planar wave
Grid 500*202, dx=dz=10m, dt=1ms
Half Space: Vp=5.02km/s, Vs=2.898km/s

Figure 10

Step 4: Plotting Synthetics

Figure 11 shows the vertical components recorded at 31 grid points on the free surface for 630 marching steps in time, with $\Delta t = 0.001$ sec. The sensors are 0.16km apart in X direction. The numerical label (at the right) indicates the distance from the corresponding sensor to the nearer corner point. Reflections from the edge would begin to contaminate the wavefield after 0.6 sec, due to the symmetric boundary conditions. This figure is generated with a utility program *"arrayplt"* using the following script. Note that we have two more utility programs *"trplt90"* and *"trplt"* which read exactly the same input parameter file to generate different types of plots (*e.g.*, Figures 14 and 16).

```
#
set nonomatch
setenv PSLANDSCAPE
#--- rotate the plot by 90 degrees

set DB=( VERT HORI )
foreach i ( 1 )
cat << EOF > input
1) job type (odd==>.w, even==>ASCII, negative==>keep error messages)
2
2) database name (char*40):
$DB[$i]
3) sampling rate
1000.0
4) # of traces to be plotted
31
5) give seismogram indices:
1 2 3 4 5 6 7 8 9 10 11 12 13 14 15 16 17 18 19 20 21 22 23 24 25 26 27 28 29 30 31
6) give starting point of each trace:
1 1 1 1 1 1 1 1 1 1 1 1 1 1 1 1 1 1 1 1 1 1 1 1 1 1 1 1 1 1 1
7) give signal window of each trace:
630 630 630 630 630 630 630 630 630 630 630 630 630 630 630 630 630 630 630 630 630 630 630 630 630 630 630 630 630 630 630
8) turn on de-spiker (>0==>yes)? turn on 98%-ile detector (>0=>yes)
0 0
9) AGC(0) or normalized by {max(1), constant(2), specific trace(3)}
2
9-2) give normalizing constant:
0.30
10) black out negative part? (>0==>yes) tic marks? ( >0 ==> yes)
1 0
11) reduced time scale? (>0 ==> yes) group velocity (dummy if .le.0)
0 10 0
12) decimation option
1
13) title
45-deg ramp, grid 500*400, dx=10m, dt=.001s, planar P wave
14) give channel ID's or distances (as many lines as # of traces)
-2.08km
-1.92km
-1.76km
-1.60km
-1.44km
```

37

```
-1.28km
-1.12km
-0.96km
-0.80km
-0.64km
-0.48km
-0.32km
-0.16km
corner1
ramp
ramp
ramp
corner2
0.16km
0.32km
0.48km
0.64km
0.80km
0.96km
1.12km
1.28km
1.44km
1.60km
1.76km
1.92km
2.08km
EOF
arrayplt < input > & error
end
```

It is interesting to note that for an incident P wave, the bottom corner of the ramp (or step) is an efficient scatterer of P waves, whereas the top corner of the inclined surface (at 45°) produces a strong scattered Rayleigh field (*cf*. Figures 10 and 11). The bottom corner has the smallest peak amplitude (*cf*. the rightmost column of Figure 11), whereas the top corner has the largest peak amplitude.
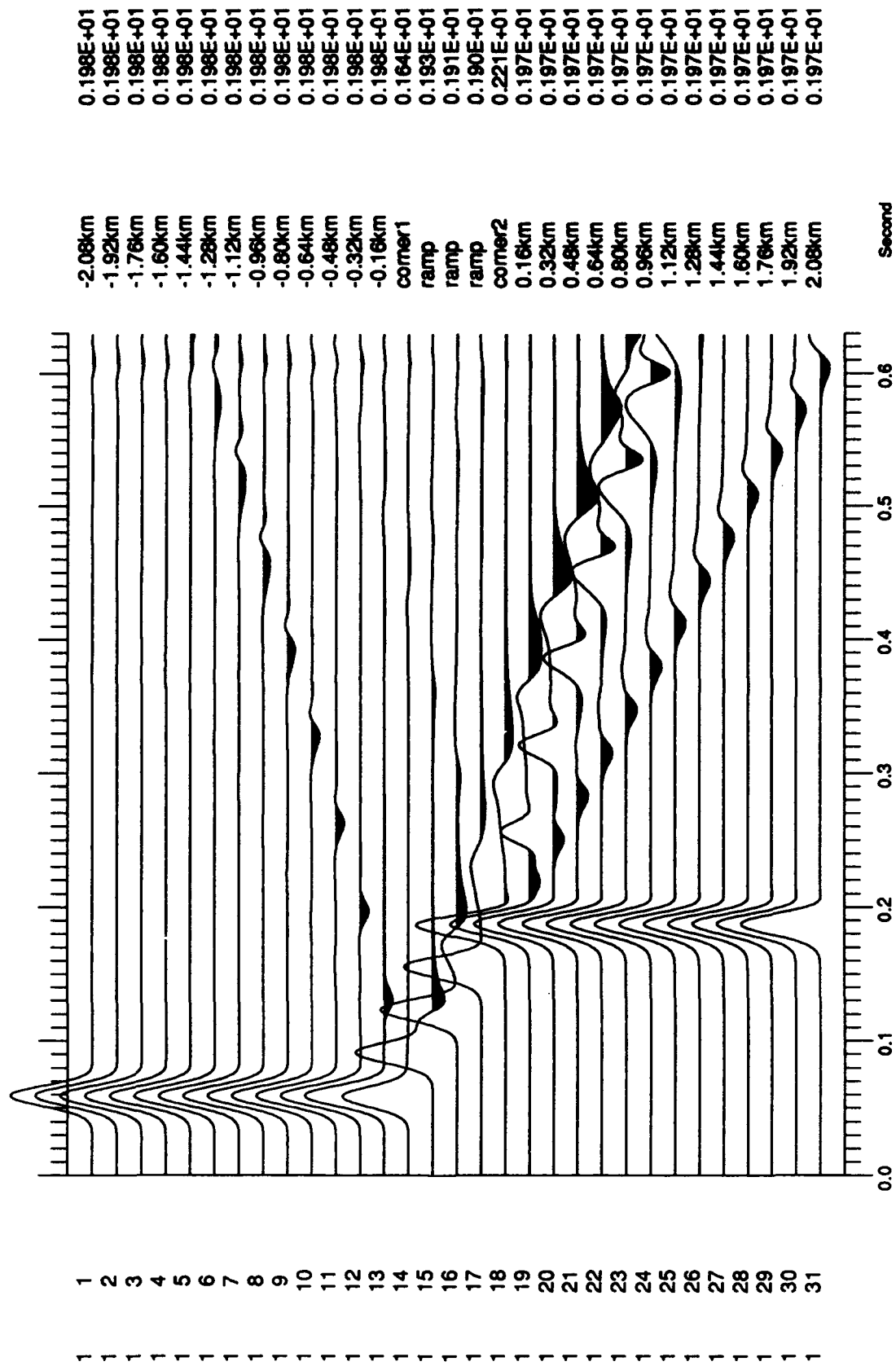
45-deg ramp, grid 500*400, dx=dz=10m, dt=.001s, planar P wave

Vertical Component
Uniform Scaling

Figure 11

July 15 1993
User: jlh
SW design: jlh 06/98

Second

1	0.198E+01
2	0.198E+01
3	0.198E+01
4	0.198E+01
5	0.198E+01
6	0.198E+01
7	0.198E+01
8	0.198E+01
9	0.198E+01
10	0.198E+01
11	0.198E+01
12	0.198E+01
13	0.198E+01
14	0.164E+01
15	0.193E+01
16	0.191E+01
17	0.190E+01
18	0.221E+01
19	0.197E+01
20	0.197E+01
21	0.197E+01
22	0.197E+01
23	0.197E+01
24	0.197E+01
25	0.197E+01
26	0.197E+01
27	0.197E+01
28	0.197E+01
29	0.197E+01
30	0.197E+01
31	0.197E+01

-2.08km
-1.92km
-1.76km
-1.60km
-1.44km
-1.28km
-1.12km
-0.96km
-0.80km
-0.64km
-0.48km
-0.32km
-0.16km
corner1
ramp
ramp
ramp
corner2
0.16km
0.32km
0.48km
0.64km
0.80km
0.96km
1.12km
1.28km
1.44km
1.60km
1.76km
1.92km
2.08km

6. EXAMPLE 2: RAYLEIGH WAVE SCATTERING AT SEDIMENTARY BASIN

The relative importance of near-surface effects versus deep-crustal effects on relative amplitudes can be examined by modeling in laterally heterogeneous models. Numerical experiments are particularly suitable to address the effects of variable crustal thickness, rugged mountainous relief, sediment thickness, and other structural heterogeneities on L_g and R_g amplitudes. Such studies would complement the empirical studies by providing better interpretations and better insight of the underlying physics. As an illustrating experiment, here we give an example to demonstrate how LFD calculations can be utilized in explaining and quantifying the R_g/L_g blockage as well as the higher Sg/S_n coda level due to strong L_g-to-S_n and R_g-to-Sg conversion at the pinched attenuating sediment layers.

The initial waveform is chosen so that the vertical displacement W on the flat free-surface is a Ricker wavelet. This wavelet has been adopted frequently in finite-difference simulations because it is well localized in both spatial and wavenumber domains (Boore, 1972; Munasinghe and Farnell, 1973; Fuyuki and Matsumoto, 1980; Fuyuki and Nakano, 1984; Levander, 1985). To avoid grid dispersion, we chose 1.2135 km = 48.5 Δx as the dominant wavelength of the incident Rayleigh wave packet in a homogeneous portion of the medium with a P-wave velocity 4.57 km/sec and Poisson's ratio 0.35. Absorbing boundary conditions (Clayton and Engquist, 1977; Emerman and Stephen, 1983) are adopted on the sides and bottom to suppress the artificial reflections from the sides of the grid. Note that the quasi-transparent boundary conditions do allow the wave to disappear into the sides and bottom of the grid.

Step 1: 2-D Model Generation

The utility program "lymed3" generates a 2-dimensional medium, of which the material properties are constant within subregions separated by (piecewise linear) polygons. It reads the coordinates of the vertices of polygons and fills the medium above the polygon with prespecified material properties. By repeating this procedure several times, this routine generates a 2-dimensional velocity model for the FD simulations. "lymed3a" and "lymed3b" produce the corresponding graphic presentation of the medium (as a PostScript output file). The only difference between these two codes is that "lymed3a" fills in each layer with shaded pattern, whereas "lymed3b" fills in each layer with a predefined pattern. The PostScript output can be then transmitted to laser printers directly.

The 1st line of the input file specifies the label (in quotes), which is followed by grid size, grid spacings, the velocity parameters of the half space, as well as the number of the polygons. "lymed3" and "lymed3a" then read exactly as many polygons as defined. Each polygon begins with the number of vertices in this particular polygon as well as the material parameters for the medium above this polygon. The material parameters are typically the compressional velocity, shear velocity, and the density, but they could also be the Lame constants. These parameters are not required for the graphic routine "lymed3a".

```
#
set nonomatch
#— job 1: run 'lymed3' to generate medium models (Vp, Vs, Rho)
#— job 2,3: run 'lymed3a/b' to generate PostScript plot of the model
set job=( lymed3 lymed3a lymed3b)
```

```
foreach i ( 3 )
cat << I > MOD.IN
600    500      (give model size: kw,kh)
0.025  0.025     (give spatial spacing: dx,dz in km)
6.15 3.5 2.8      (give Vp,Vs,Rho in half space)
4               (how many interfaces/layers)
2 4.57 2.64 2.5      (# of points of interface 1; Vp,Vs,Rho above it)
1    122         (1st vertex of interface 1)
600  122          (2nd vertex of interface 1)
4 3.00 1.60 2.25     (# of points of interface 2; VP,Vs,Rho above it)
160  2           (1st vertex of interface 2)
280  62           (2nd vertex of interface 2)
320  62              (....)
440  2              (....)
4 2.140 1.143 2.000
160  2
220  32
380  32
440  2
4 1.340 0.640 1.800
160  2
240  12
360  12
440  2
I
$job[$i] < MOD.IN
end
```

Program *"lymed3b"* generates the following output message as well as a *PostScript* formatted file
which can be directed to the laser printer for a hard copy of the model (Figure 12).

```
LYMED3B, 930508 RSJ
"Sedimentary Basin (model E3)"
lymed3b> grid size: 600  500
lymed3b> mesh widths:    .0250    .0250
lymed3> half-space parameters (alpha, beta, rho):     6.150      3.500      2.800
lymed3b> # of interfaces:  4
 interface  1 has   2 vertices
 with Vp,Vs,Rho above this interface:    4.5700    2.6400    2.5000
 interface  2 has   4 vertices
 with Vp,Vs,Rho above this interface:    3.0000    1.6000    2.2500
 interface  3 has   4 vertices
 with Vp,Vs,Rho above this interface:    2.1400    1.1430    2.0000
 interface  4 has   4 vertices
 with Vp,Vs,Rho above this interface:    1.3400     .6400    1.8000
total x,z (km)=  .15000E+02  .12500E+02
Xscale,ddx,xlngth=     .3333    .0083    5.0000
Zscale,ddz,zlngth=    -.2400   -.0060   -3.0000

Interface   1 (from bottom)
     4 revised Jordan vertices:
```

41

```
Vp,Vs,Rho=    4.570    2.640    2.500
        1        0
        1      120
      600      120
      600        0

Interface   2 (from bottom)
    4 revised Jordan vertices:
Vp,Vs,Rho=    3.000    1.600    2.350
      160        0
      280       60
      320       60
      440        0

Interface   3 (from bottom)
    4 revised Jordan vertices:
Vp,Vs,Rho=    2.140    1.143    2.000
      160        0
      220       30
      380       30
      440        0

Interface   4 (from bottom)
    4 revised Jordan vertices:
Vp,Vs,Rho=    1.340     .640    1.800
      160        0
      240       10
      360       10
      440        0
```
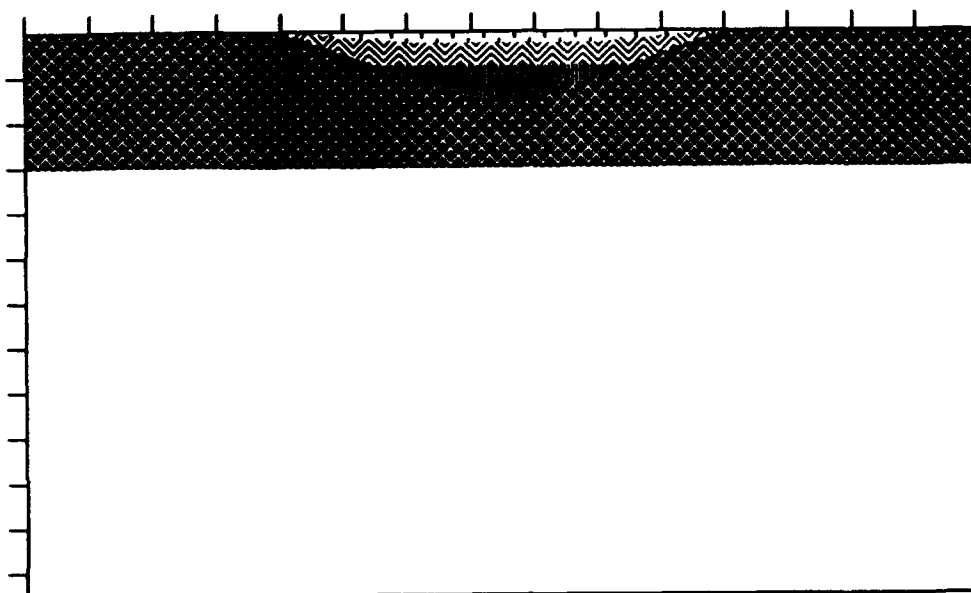
'Sedimentary Basin (model E3)'

(only uppermost layers are shown)

DX= .0250Km , DZ= .0250Km

X tic mark = Z tic mark =   1km

Half space parameters: 6.150   3.500   2.800

Interface 1 from bottom: 4.570   2.640   2.500
        4   revised Jordan vertices:
        (1 ,   0)   (1 , 120)   (600 , 120)   (600 ,   0)

Interface 2 from bottom: 3.000   1.600   2.250
        4   revised Jordan vertices:
        (160 ,   0)   (280 ,   60)   (320 ,   60)   (440 ,   0)

Interface 3 from bottom: 2.140   1.143   2.000
        4   revised Jordan vertices:
        (160 ,   0)   (220 ,   30)   (380 ,   30)   (440 ,   0)

Interface 4 from bottom: 1.340   .640   1.800
        4   revised Jordan vertices:
        (160 ,   0)   (240 ,   10)   (360 ,   10)   (440 ,   0)

Figure 12

Step 2: Running FD

```
#
set nonomatch
cat << EOF > input
grid dimension kw,kh
600 500
x,z spacings of the grid mesh & temporal spacing: dx,dz,dt
0.025 0.025 0.0025
homogeneous or heterogeneous (0,1,2)
2
inVp
inVs
inRho
topography model, inTOP
none
choose wave type
4
alpha, i0,j0, wvlns
360.00 80 20 1.2135
the option for snapshot display: component,AGC,begin & end column
"M" 1
  1 600   1 4001 22  200
  1   0   1 3001 22  500
301   0 361  721 1  100
401   0 601  961 1  100
401   0 901 1261 1  100
401   0 1201 1561 1  100
101   0 1381 1801 1  100
301   0 1681 2161 1  100
401   0 1941 2341 1  100
stations for recording seismograms
30
coordinates of sensors: (line 1 = X's, line 2 = Z's)
040 080 120 160 200 240 280 320 360 400 440 480 520 560 600
040 080 120 160 200 240 280 320 360 400 440 480 520 560 600
002 002 002 002 002 002 002 002 002 002 002 002 002 002 002
200 200 200 200 200 200 200 200 200 200 200 200 200 200 200
total number of iterations; iteration/snapshot
4001 200
marching grid, total size
0 600
EOF

fd2 < input > & FD2_msg
fdsplt < data.0 > & Error_msg
```

Step 3: Generating Snapshots

L_g and R_g are susceptible to sedimentary basin structures and other types of lateral heterogeneity such as mountainous topography. The scattering at the edge of a pinched attenuating basin could be very severe, as illustrated in these snapshots of the displacement wavefield. Snapshot 3 indicates that the incident R_g generates higher modes in the basin, followed by slower fundamental mode Rayleigh waves, as well as the converted body waves. Note that a large bulk of the converted S wave energy tunnels underneath the basin. In snapshot 5, another strong Rayleigh-to-S conversion at the edge of the basin is clearly visible. This LFD example can be scaled to explain the L_g blockage by Barents Shelf as well as the high S_n coda level observed at NORESS due to strong L_g-to-S_n conversion reported by Baumgardt (1991).

```
#
set nonomatch
cat << ! > Lfile
4
2
1    122
600   122
4
160  2
280   62
320   62
440   2
4
160   2
220   32
380   32
440   2
4
160   2
240   12
360   12
440   2
!
cat << ! > Label
Sedimentary Basin (model E3)
600*500 [dx=25m,dt=2.5ms]
Rg: 1.2135km, 2Hz
!

#— 0,1,3,6,10 sec
set kk = ( S1004 S1014 S1034 S1064 S1104 )
foreach i ( 1 2 3 4 5 )
#— change label
ex $kk[$i] << EOF >> junk
4,6d
3
r Label
1
w!
```

```
q
EOF
end

#--- plot out snapshots
movie     -i 3 -l Lfile -m 5 $idk > & error
#movie -t -i 3 -l Lfile -m 5 $idk > & error
#movie -v -i 2 -l Lfile -m 5 $idk > & error
```

FD step   0

SQRT(V**2+H**2) 0.000SEC,   1 600 1 200

X Tic Mark =   1 Unit; Z Tic Mark =   1 Unit

.00000E+00 .12975E+01

FD step 400

SQRT(V**2+H**2) 1.000SEC,   1 600 1 200

X Tic Mark =   1 Unit; Z Tic Mark =   1 Unit

.00000E+00 .77114E+00

FD step 1200

SQRT(V**2+H**2) 3.000SEC,   1 600 1 200

X Tic Mark =   1 Unit; Z Tic Mark =   1 Unit

.00000E+00 .31152E+00

FD step 2400

SQRT(V**2+H**2) 6.000SEC,   1 600 1 200

X Tic Mark =   1 Unit; Z Tic Mark =   1 Unit

.00000E+00 .28379E+00

FD step 4000

SQRT(V**2+H**2) 10.000SEC,   1 600 1 200

X Tic Mark =   1 Unit; Z Tic Mark =   1 Unit

.00000E+00 .85667E-01

Sedimentary Basin (model E3)
600*500 [dx=25m,dt=2.5ms]
Rg: 1.2135km, 2Hz

Figure 13

Step 4: Plotting Synthetics

```
#=== script for 'arrayplt' or 'trplt90': to plot out a bunch of traces
set nonomatch
setenv PSLANDSCAPE
set DB=( VERT )
foreach i ( 1 )

cat << EOF > input
1) job type (odd==>.w, even==>ASCII, negative==>keep error messages)
2
2) database name (char*40):
$DB[$i]
3) sampling rate
400.0
4) # of traces to be plotted
15
5) give seismogram indices:
1 2 3 4 5 6 7 8 9 10 11 12 13 14 15
6) give starting point of each trace:
1 1 1 1 1 1 1 1 1 1 1 1 1 1 1 1 1 1 1 1 1 1 1 1 1 1 1 1 1 1 1 1 1 1 1 1
7) give signal window of each trace:
5000 5000 5000 5000 5000 5000 5000 5000 5000 5000 5000 5000 5000 5000 5000 5000 5000 5000 5000 5000
8) turn on de-spiker (>0==>yes)? turn on 98%-ile detector (>0=>yes)
0 0
9) AGC(0) or normalized by ( max(1), constant(2), specific trace(3))
1
9-0) give normalizing constant:
1 1 1 1 1 1 1 1 1 1 1 1 1 1 1 1 1 1 1 1 1 1 1 1 1 1 1 1 1 1 1 1 1 1 1 1
10) black out negative part? (>0==>yes) tic marks? ( >0 ==> yes)
0 0
11) reduced time scale? (>0 ==> yes) group velocity (dummy if .le.0)
0 10 0
12) decimation option
1
13) title
Rg; sedimentary basin (model E3)
14) give channel ID's or distances (as many lines as # of traces)
-3km
-2km
-1km
0km_B
1km_B
2km_B
3km_B
4km_B
5km_B
6km_B
7km_B
+1km
+2km
+3km
+4km
```

```
EOF
trplt90 < input > & error
rm input TRPLT*
end
```
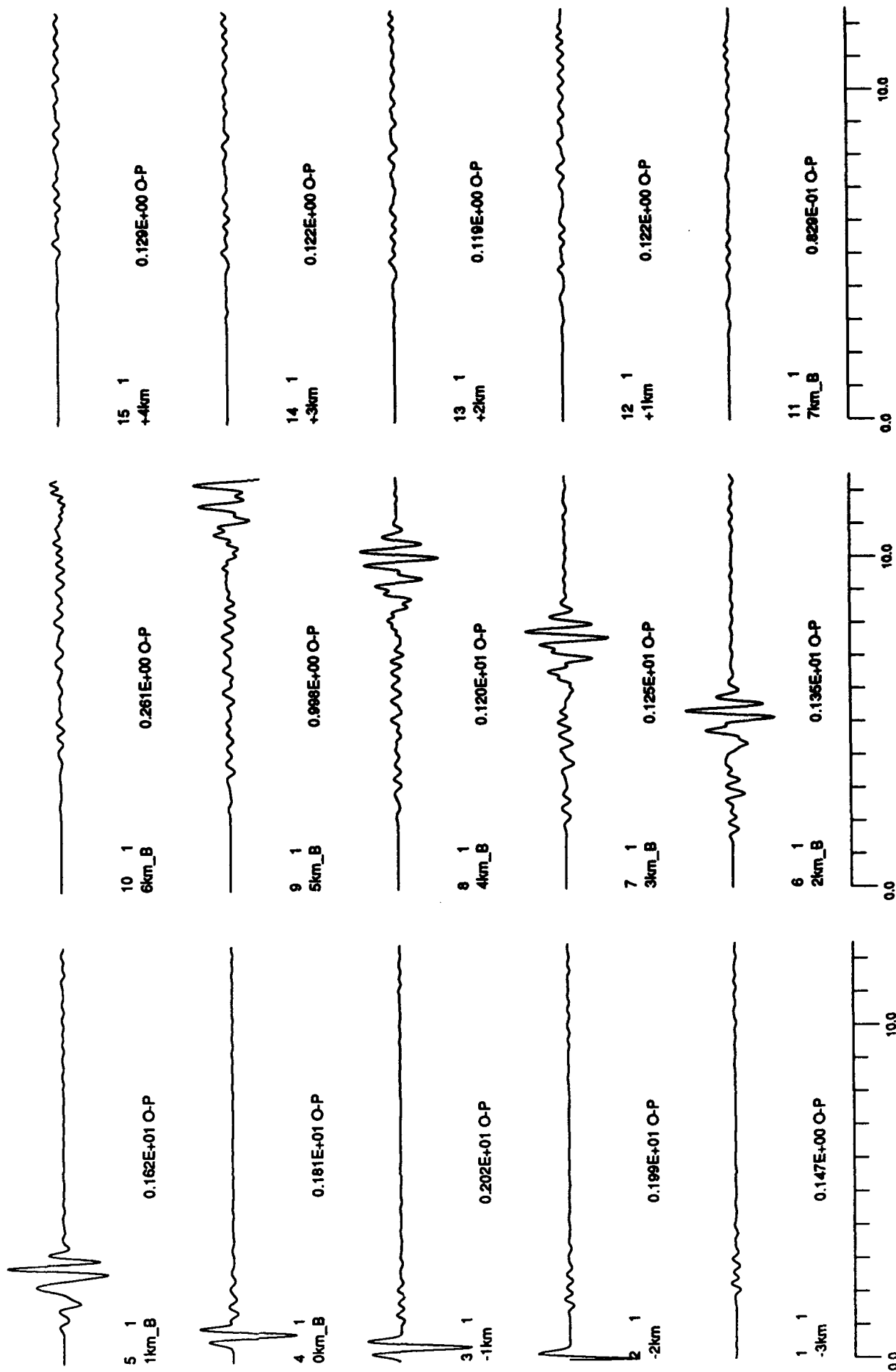
Rg; sedimentary basin (model E3)

Uniform scale

Figure 14

7. EXAMPLE 3: RIPPLE FIRING

A major issue for the Non-Proliferation Treaty is the discrimination of large chemical explosions from possible clandestine or small nuclear tests. Unless discrimination is possible, the numerous mining blasts could provide ample opportunity for concealing clandestine tests. Rippled-fired explosions are commonly used to fragment rocks during quarry and open-pit mining. The periodicity inherent in the ripple firing could produce a seismic reinforcement at the frequency of the delay between shots or rows. It has been suggested that the convolution of a single explosion with a comb function of variable spacing and variable amplitude can be used to model the distinctive signature of ripple firing (Stump, 1988; Anderson and Stump, 1989; Smith, 1989; Hedlin *et al.*, 1990; Chapman *et al.*, 1992; Reamer *et al.*, 1992; and many others). Baumgardt and Ziegler (1988) delicately demonstrated that the incoherent array-stack spectra can be used to identify some multiple shots recorded at NORSAR. By superpositioning the waveform due to a single shot with proper time delay, they were able to model the source multiplicity under the assumption that the spatial spreading of the shots is negligible with respect to the distance to the receiver. The work by Stump *et al.* successfully characterized the major features of the wavefield due to ripple firings at near-source ranges.

There are, however, some other wave excitation characteristics of ripple-fired explosions which are not predicted by such spectral or waveform superposition approaches. In this example, the linear finite-difference (LFD) method is utilized to seek some insights into the ripple-fired explosions.

The preliminary results suggest that ripple firing could excite directionally dependent R_g and S^*. Thus the lack of R_g may not be always indicative of a deep source. Rather, it could also be due to the shot pattern. However, the enhanced R_g in the forward direction of ripple firing can be strongly attenuated by lateral heterogeneity and surface topography. The scattered R_g energy could then couple into the crustal waveguide as L_g and other phases (McLaughlin and Jih, 1986, 1987; Jih and McLaughlin, 1988). Since such scattering mechanisms are commonly present in many quarry sites or mines, it is not surprising that the directional enhancement of R_g may not be always observable. The spall could obscure the azimuthal dependency of R_g as well. Previous LFD modeling studies (McLaughlin and Jih, 1986, 1987) suggest that the near-source R_g-to-S scattering is usually stronger than that of R_g-to-P, which could provide a plausible explanation of why quarry blasts and mining blasts should discriminate less well from earthquakes than would contained nuclear explosions. Further quantitative analysis along this line could be very useful.

Step 1: Model Generation

Suppose we want to test 7 ripple-fired explosions in a model with a trapezoidal topography. The whole grid has a dimension of 800 by 600 nodes with the topography embedded in the central portion. The following sample script generates the topography file for the nominal model in which we set off the ripple fires from left to right. The topography starts with a flat segment of 350 grids, a 45° ramp of 30 grids high, a plateau of 100 grids long, a -45° ramp of 30 grids long, and followed by a flat segment of 290 grids. To make sure that the topography is shown in the central portion of the snapshots, we will extract the wavefield from columns 231 to 630. The topography for the flipped model would have a reversed order, and we will extract from columns 171 to 570.

51

```
#
cat << / > inTOP,right
32
00 00 00 00 00 00 00 00 00 00 00 00 00 00 00 00 00 00 00 00 00 00 00 00 00 00 00 00 00 00 00 00
00 00 00 00 00 00 00 00 00 00 00 00 00 00 00 00 00 00 00 00 00 00 00 00 00 00 00 00 00 00 00 00
00 00 00 00 00 00 00 00 00 00 00 00 00 00 00 00 00 00 00 00 00 00 00 00 00 00 00 00 00 00 00 00
00 00 00 00 00 00 00 00 00 00 00 00 00 00 00 00 00 00 00 00 00 00 00 00 00 00 00 00 00 00 00 00
00 00 00 00 00 00 00 00 00 00 00 00 00 00 00 00 00 00 00 00 00 00 00 00 00 00 00 00 00 00 00 00
00 00 00 00 00 00 00 00 00 00 00 00 00 00 00 00 00 00 00 00 00 00 00 00 00 00 00 00 00 00 00 00
00 00 00 00 00 00 00 00 00 00 00 00 00 00 00 00 00 00 00 00 00 00 00 00 00 00 00 00 00 00 00 00
00 00 00 00 00 00 00 00 00 00 00 00 00 00 00 00 00 00 00 00 00 00 00 00 00 00 00 00 00 00 00 00
00 00 00 00 00 00 00 00 00 00 00 00 00 00 00 00 00 00 00 00 00 00 00 00 00 00 00 00 00 00 00 00
00 00 00 00 00 00 00 00 00 00 00 00 00 00 00 00 00 00 00 00 00 00 00 00 00 00 00 00 00 00 00 00
00 00 00 00 00 00 00 00 00 00 00 00 00 00 00 00 00 00 00 00 00 00 00 00 00 00 00 00 00 00 00 00
00 00 00 00 00 00 00 00 00 00 00 00 00 00 00 00 00 00 00 00 00
01 02 03 04 05 06 07 08 09 10 11 12 13 14 15 16 17 18 19 20 21 22 23 24 25 26 27 28 29 30
30 30 30 30 30 30 30 30 30 30 30 30 30 30 30 30 30 30 30 30 30 30 30 30 30 30 30 30 30 30 30
30 30 30 30 30 30 30 30 30 30 30 30 30 30 30 30 30 30 30 30 30 30 30 30 30 30 30 30 30 30 30
30 30 30 30 30 30 30 30 30 30 30 30 30 30 30 30 30 30 30 30 30 30 30 30 30 30 30 30 30 30 30
30 30 30 30 30 30 30 30 30 30
30 29 28 27 26 25 24 23 22 21 20 19 18 17 16 15 14 13 12 11 10 09 08 07 06 05 04 03 02 01
00 00 00 00 00 00 00 00 00 00 00 00 00 00 00 00 00 00 00 00 00 00 00 00 00 00 00 00 00 00 00 00
00 00 00 00 00 00 00 00 00 00 00 00 00 00 00 00 00 00 00 00 00 00 00 00 00 00 00 00 00 00 00 00
00 00 00 00 00 00 00 00 00 00 00 00 00 00 00 00 00 00 00 00 00 00 00 00 00 00 00 00 00 00 00 00
00 00 00 00 00 00 00 00 00 00 00 00 00 00 00 00 00 00 00 00 00 00 00 00 00 00 00 00 00 00 00 00
00 00 00 00 00 00 00 00 00 00 00 00 00 00 00 00 00 00 00 00 00 00 00 00 00 00 00 00 00 00 00 00
00 00 00 00 00 00 00 00 00 00 00 00 00 00 00 00 00 00 00 00 06 00 00 00 00 00 00 00 00 00 00 00
00 00 00 00 00 00 00 00 00 00 00 00 00 00 00 00 00 00 00 00 00 00 00 00 00 00 00 00 00 00 00 00
00 00 00 00 00 00 00 00 00 00 00 00 00 00 00 00 00 00 00 00 00 00 00 00 00 00 00 00 00 00 00 00
00 00 00 00 00 00 00 00 00 00 00 00 00 00 00 00 00 00 00 00 00 00 00 00 00 00 00 00 00 00 00 00
00 00 00 00 00 00 00 00 00 00 00 00 00 00 00 00 00 00 00 00 00 00 00 00 00 00 00 00 00 00 00 00
00 00 00 00 00 00 00 00 00 00 00 00 00 00 00 00 00 00 00 00 00 00 00 00 00 00 00 00 00 00 00 00
00 00 00 00 00 00 00 00 00 00 00 00 00 00 00 00 00 00 00 00 00 00 00 00 00 00 00 00 00 00 00 00
00 00 00 00 00 00 ^0 00 00 00 00 00 00 00 00 00 00 00 00 00 00 00 00 00 00 00 00 00 00 00 00 00
00 00 00 00 00 ഫ )0 00 00 00 00 00 00 00 00 00 00 00 00 00 00 00 00 00 00 00 00 00 00 00 00 00
00 00 00 00 00 00 00 00 00 00 00 00 00 00 00 00 00 00 00 00 00 00 00 00 00 00 00 00 00 00 00 00
00 00 00 00 00 00 00 00 00 00 00 00 00 00 00 00 00 00 00 00 00 00 00 00 00 00 00 00 00 00 00 00
/
```

Step 2: Running FD

For the nominal model, the 7 sources are located at <385,5>, <390,5>, <395,5>, <400,5>, <405,5>, <410,5>, and <415,5>. Except the first shot, which is detonated at time step 0, the remaining 6 explosions are detonated at 20 time steps apart (*cf.* the parameter file below). For the flipped model, we reverse the order to set off the first shot at time step 0 at grid point <415,5>. In the nominal model, we show the wavefield between columns 231 and 630, whereas for the flipped model, we show the grid between columns 171 and 570. Thus once we flip the model back, both runs will be showing physically the same portion of the wavefield.

```
#— for nominal model
set nonomatch
#need: DRIVER5

# generate input parameter file for fd
cat << EOF > inFD
1) grid dimension kw,kh
800 600
2) x,z spacings of the grid mesh & temporal spacing: dx,dz,dt
0.01 0.01 0.001
3) homogeneous (0), heterogeneous (1,2)
0
inVp
inVs
inRho
4) topography file
inTOP
5) choose wave type
9
5-1) driver file
DRIVER5
5-2) how many ripples
7
020 390 5
040 395 5
060 400 5
080 405 5
100 410 5
120 415 5
6) alpha, i0,j0, wvlns
20.00 385 5 0.2
7) option for snapshot display: component,AGC,begin & end column
"v" 1
   1 800    1 5201 22 240
 231 630    1 2201 22 120
 201   00   1 5001 2 600
 301   00  801 2000 2 250
 701   00  901 1261 2 100
 901   00 1201 1561 2 100
1101   00 1381 1801 2 100
1301   00 1681 2161 2 100
```

```
1501   00 1941 2341 2 100
8) # of seismographs
18
9) coordinates of sensors: (line 1=X's,line 2=Z's,negX=strain sensor)
001 100 200 300 400 500 600 700 800 001 100 200 300 400 500 600 700 800
032 032 032 032 002 032 032 032 032 002 002 002 002 002 002 002 002 002
10) total # of iterations; # of iterations/snapshot
4201 100
11) marching grid (>0==>yes)? total grid width desired:
400 1200
EOF

fd2 < inFD > & FD_mag
```

Step 3: Generating Snapshots

In the input parameter file for "fd2", we specified two subgrids for snapshot output (*cf.* the discussion in Step 2). The following is a sample script for generating the snapshots of the central portion only. Note that the topography radiates the fundamental Rayleigh-wave energy into body waves of much lower frequency, as shown at 0.5 and 0.7 sec. Part of the Rayleigh-wave energy is trapped between the two ramps (*cf.* 0.6 and 0.7 sec) and eventually scattered into the coda waves. The topography attenuates the Rayleigh wave in both directions dramatically and produces a more complex waveform.

```
#
set nonomatch
#-- 2 types: Right (for nominal model), Left (for flipped model)
set type=( Right )

cat << EOF > Label
7 shallow ripple-fired shots
Trapezoidal topography
Vp=5.02km/s, Vs=2.898km/s
EOF
cat << I > Tmp
385 5
390 5
395 5
400 5
405 5
410 5
415 5
I
if ($type == 'Left' ) then
set move=( 170 )
          cat << I > flipwf.f
          program flipwf
C======= 930304: flip over character fields
          character*800 A,B
          character*10 label
          read(5,'(a10,2i5)')label,long,mn
          write(6,'(a10,2i5)')label,long,mn
          do i=1,11
            read(5,'(a)')A
            ijk=lnblnk(A)
            write(6,'(a)')A(1:ijk)
          end do
100       read(5,'(a)',end=200)A
          do i=1,long
           j=long+1-i
            B(i:i)=A(j:j)
          end do
          write(6,'(a)')B(1:long)
          go to 100
200       stop
          end
```

```
/
        make flipwf
else
        set move=( 230 )
endif
echo $move

set idx=( S2001 S2003 S2005 S2007 S2009 )
set jj=( M1 M2 M3 M4 M5 )
foreach i ( 1 2 3 4 5 )
#— change label
if ( $type == 'Left' ) then
        flipwf < $idx[$i] > $jj[$i]
else
        cp $idx[$i] $jj[$i]
endif
ex $jj[$i] << EOF >> Junk
4,6d
3
r Label
1
wq
EOF
end

rm ps*
cat << I > DO
awk '{print -$move,}' < Tmp > Rfile
I
csh DO ; rm DO

#— plot out snapshots
movie -t -I 3 -r Rfile -m 5 $jj > & Error
```
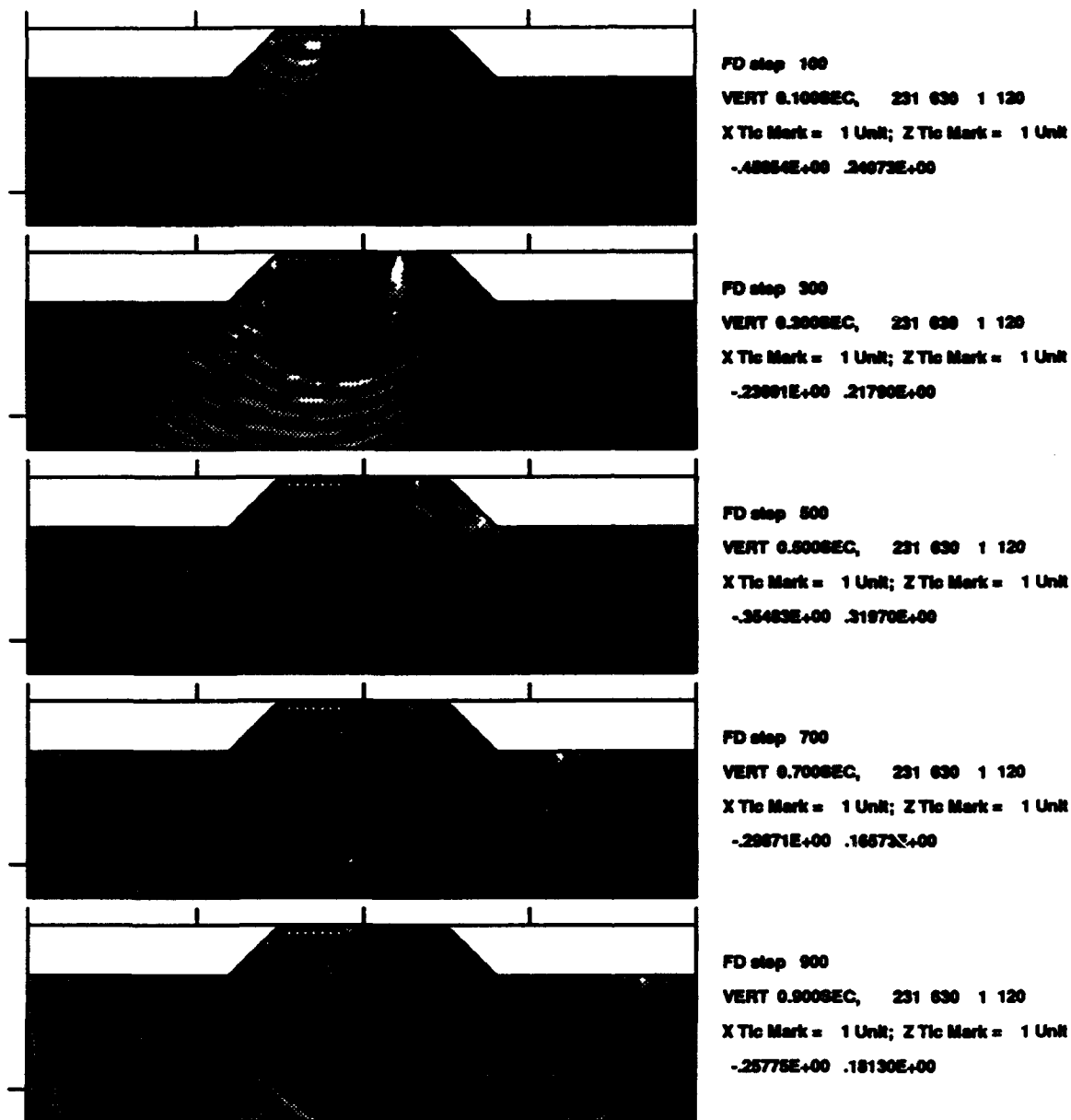
FD step 100

VERT 0.100SEC,   231 630   1 120

X Tic Mark =   1 Unit; Z Tic Mark =   1 Unit

 -.49954E+00 .24073E+00

FD step 300

VERT 0.300SEC,   231 630   1 120

X Tic Mark =   1 Unit; Z Tic Mark =   1 Unit

 -.23991E+00 .21790E+00

FD step 500

VERT 0.500SEC,   231 630   1 120

X Tic Mark =   1 Unit; Z Tic Mark =   1 Unit

 -.35453E+00 .31970E+00

FD step 700

VERT 0.700SEC,   231 630   1 120

X Tic Mark =   1 Unit; Z Tic Mark =   1 Unit

 -.29071E+00 .16573E+00

FD step 900

VERT 0.900SEC,   231 630   1 120

X Tic Mark =   1 Unit; Z Tic Mark =   1 Unit

 -.25775E+00 .15130E+00

7 shallow ripple-fired shots
Trapezoidal topography
Vp=5.02km/s, Vs=2.898km/s

Figure 15

Step 4: Merging Synthetics

As specified in the sample input parameter file for "fd2" (page 53), the original grid size was defined as 800x600. As soon as the wavefront gets close to the edge, the program "fd2" shifts the grid laterally by 400 grid points (*cf.* the line marked "marching grid"), and it starts to save the synthetics in another buffer called "data.1" (as opposed the the nominal buffer "data.0"). Since the total grid width desired was 1200 (= 800 + 400) points, only one shift would be required. At the end of the LFD run, we need to merge the synthetics according to their physical locations. The following script assumes that the buffers "data.0" and "data.1" are stored in separate directories "Data.1" and "Data.2", respectively. The demultiplexer routine "fdsplt" is called twice to decode the synthetics in these two directories. Synthetics associated with the same location are then merged (or zero-filled) and renamed.

```
#
set nonomatch
foreach i ( Left )
foreach j ( 1 2 )
cd $i/Data_$j
if ( -e data.* ) then
        uncompress data.*.Z
        fdsplt < data* > & Error
        compress VERT*
        rm Error HORI*
endif
cd $where
end
end

cat << ! > ZERO_25
0 0 0 0 0 0 0 0 0 0 0 0 0 0 0 0 0 0 0 0 0 0 0 0 0
!
cat ZERO_25 ZERO_25 ZERO_25 ZERO_25 > ZERO_100
cat ZERO_100 ZERO_100 > ZERO_200
cat ZERO_200 ZERO_200 ZERO_200 ZERO_200 > ZERO_800
cat ZERO_800 ZERO_100 > ZERO_900
rm Z.*

#=== left
@ i = 1
zcat Left/Data_1/VERT.8.Z Left/Data_2/VERT.4.Z > Z.$i
@ i = $i + 1
cp ZERO_800 Z.$i ; zcat Left/Data_2/VERT.6.Z >> Z.$i
@ i = $i + 1
cp ZERO_800 Z.$i ; zcat Left/Data_2/VERT.8.Z >> Z.$i

#=== right
@ i = $i + 1
zcat Right/Data_1/VERT.8.Z Right/Data_2/VERT.4.Z > Z.$i
@ i = $i + 1
cp ZERO_900 Z.$i ; zcat Right/Data_2/VERT.6.Z >> Z.$i
@ i = $i + 1
cp ZERO_900 Z.$i ; zcat Right/Data_2/VERT.8.Z >> Z.$i
```
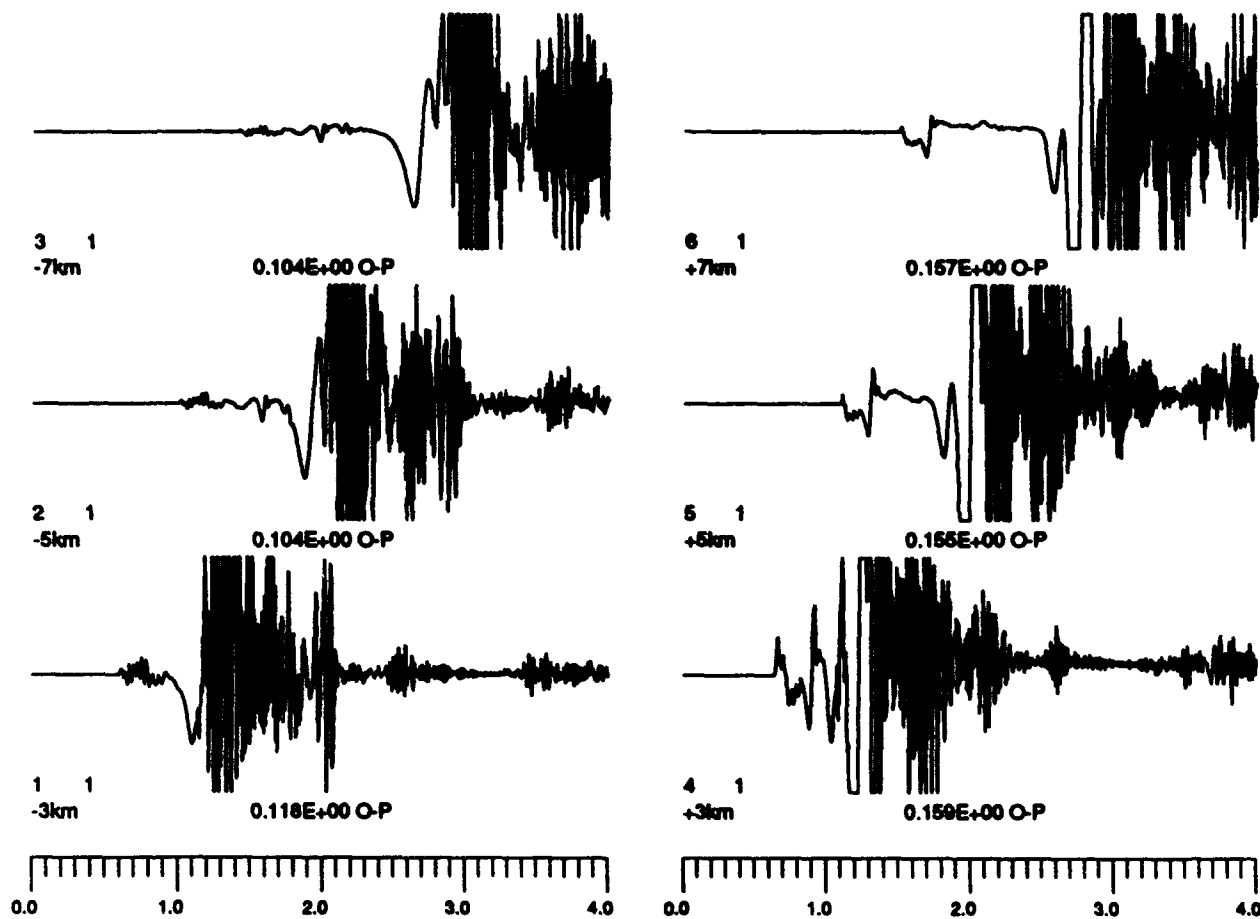
58

rm ZERO*

Step 5: Plotting Synthetics

The combined synthetics are then plotted out with yet another plotting routine "*trplt*", which plots the traces in two columns. In this case, no rotating of the plot is required. Note that "*trplt*" reads the same format of input parameter file as do "*arrayplt*" and "*trplt90*".

```
#=== script for 'trplt' --- to plot out a bunch of traces
set nonomatch
set DB=( Z VERT )
foreach i ( 1 )

cat << EOF > input
1) job type (odd==>.w, even==>ASCII, negative==>keep error messages)
2
2) database name (char*40):
$DB[$i]
3) sampling rate
1000.0
4) # of traces to be plotted
10
5) give seismogram indices:
1 2 3 3 3 4 5 6 6 6
6) give starting point of each trace:
1 1 1 1 1 1 1 1 1 1 1 1 1 1 1 1 1 1 1 1 1 1 1 1 1 1 1 1 1 1 1 1 1 1 1 1 1 1 1 1 1
7) give signal window of each trace:
4000 4000 4000 4000 4000 4000 4000 4000 4000 4000
8) turn on de-spiker (>0==>yes)? turn on 96%-ile detector (>0==>yes)
0 0
9) AGC(0) or normalized by ( max(1), constant(2), specific trace(3) )
2
9-0) give normalizing constant:
0.025 0.025 0.025 0.025 0.025 0.025 0.025 0.025 0.025 0.025 0.025 0.025 0.025 0.025 0.025 0.025 0.025
10) black out negative part? (>0==>yes) tic marks? ( >0 ==> yes)
0 0
11) reduced time scale? (>0 ==> yes) group velocity (dummy if .le.0)
0 10 0
12) decimation option
2
13) title
Trapezoid, 7 shallow ripple-fired blasts
14) give channel ID's or distances (as many lines as # of traces)
-3km
-5km
-7km
-7km
-7km
+3km
```

59

```
+5km
+7km
+7km
+7km
EOF
trplt < input > & error
end
```

3   1
-7km   0.104E+00 O-P

6   1
+7km   0.157E+00 O-P

2   1
-5km   0.104E+00 O-P

5   1
+5km   0.155E+00 O-P

1   1
-3km   0.118E+00 O-P

4   1
+3km   0.159E+00 O-P

0.0   1.0   2.0   3.0   4.0   0.0   1.0   2.0   3.0   4.0

Trapezoid, 7 shallow ripple-fired blasts

Uniform scale 0.5 inch = .2500E-01 in Y
Decimated by 2

Figure 16

Jul 21 1993

User: jlh

SW design: jlh 02/89

8. REFERENCES

For the user's convenience, references are hereby divided into three categories:

(1) publications directly used in coding "fd2",

(2) TGAL's research that utilized "fd2" or its earlier versions, and

(3) other general references.

All Teledyne Geotech reports are available through National Technical Information Service.

References Directly Used In Coding fd2

Boore, D. (1970). Love waves in nonuniform wave guides: finite-difference calculations, *J. Geophys. Res.*, **75**, 1512-1527.

Clayton, R. and B. Engquist (1977). Absorbing boundary conditions for acoustic and elastic wave equations, *Bull. Seism. Soc. Am.*, **67**, 1529-1540.

Emerman, S. and R. Stephen (1983). Comment on "Absorbing boundary conditions for acoustic and elastic wave equations" by R. Clayton and B. Engquist, *Bull. Seism. Soc. Am.*, **73**, 661-665.

Frankel, A. and R. W. Clayton (1986). Finite-difference simulation of seismic scattering: implications for the propagation of short-period seismic waves in the crust and models of crustal heterogeneity, *J. Geophys. Res.*, **91**, 6465-6489.

Jih, R.-S., K. L. McLaughlin, and Z. A. Der (1988). Free boundary conditions of arbitrary polygonal topography in a 2-D explicit elastic finite difference scheme, *Geophysics*, **53**, 1045-1055.

Kelly, K. R., R. W. Ward, S. Treitel, and M. Alford (1976). Synthetic seismograms: a finite-difference approach, *Geophysics*, **41**, 2-27.

Munasinghe, M. and G. Farnell (1973). Finite-difference analysis of Rayleigh wave scattering at vertical discontinuities, *J. Geophys. Res.*, **78**, 2454-2466.

Vidale, J. E., and D. V. Helmberger (1987), Path effects in strong motion seismology, in *Methods of Computational Physics: Strong Ground Motion Synthetics*, **4**, 267-319, Academic Press, New York.

Selected TGAL's Work Related to LFD

Der, Z. A., E. M. McElfresh, C. P. Mrazek, D. P. J. Racine, B. W. Barker, A. H. Chaplin, and H. M. Sproules (1978). Results of the NTS experiment, Phase-II, *Report SDAC-TR-78-4*, Teledyne Geotech, Alexandria, VA.

Jih, R.-S. (1993). Directional excitation of Rg due to ripple-fired explosions: 2-dimensional finite-difference calculations, *DoE/LANL Numerical Modeling for Underground Nuclear Test Monitoring Symposium, March 23-25, Durango, CO*.

Jih, R.-S., C. S. Lynnes, D. W. Rivers, and I. N. Gupta (1989). Simultaneous modeling of teleseismic and near regional phases with linear finite-difference method (abstract), *EOS, Trans. Am. Geophys. Union*, **70-43**, 1189.

Jih, R.-S. and K. L. McLaughlin (1988). Investigation of explosion generated SV Lg waves in 2-D heterogeneous crustal models by finite-difference method, *Report AFGL-TR-88-0025 (=TGAL-88-01)*, Air Force geophysics Laboratory, Hanscom Air Force base, MA.

Jih, R.-S., K. L. McLaughlin, and Z. A. Der (1988). Free boundary conditions of arbitrary polygonal topography in a 2-D explicit elastic finite difference scheme, *Geophysics*, 53, 1045-1055.

McLaughlin, K. L., L. M. Anderson, and A. C. Lees (1988). Effects of geologic structure on Yucca Flats, NTS, explosion waveforms: 2-dimensional linear finite-difference simulations, *Bull. Seism. Soc. Am.*, 77, 1211-1222.

McLaughlin, K. L., L. M. Anderson, and Z. A. Der (1985). Investigation of scattering and attenuation of seismic waves using 2-dimensional finite-difference calculations, in the *Symposium on Scattering of Waves in Random Media and Rough Surfaces*, 795-821, Varadan and Varadan editors.

McLaughlin, K. L. and R.-S. Jih (1986). Finite-difference simulations of Rayleigh wave scattering by 2-D rough topography, *Report AFGL-TR-86-0269 (= TGAL-86-09)*, Air Force geophysics Laboratory, Hanscom Air Force base, MA.

McLaughlin, K. L. and R.-S. Jih (1987). Finite-difference simulations of Rayleigh wave scattering by shallow heterogeneity, *Report AFGL-TR-87-0322 (= TGAL-87-02)*, Air Force geophysics Laboratory, Hanscom Air Force base, MA.

McLaughlin, K. L. and R.-S. Jih (1988). Scattering from near-source topography: teleseismic observations and numerical 2D explosive line sources simulations, *Bull. Seismo. Soc. Am.*, 78, 1399-1414.

General References

Alterman, Z. and F. C. Karal (1968). Propagation of elastic waves in layered media by finite difference methods, *Bull. Seism. Soc. Am.*, 58, 367-398.

Alterman, Z. and D. Loewenthal (1970). Seismic waves in a quarter and three quarter plane, *Geophys. J. R. astr. Soc.*, 20, 101-126.

Alterman, Z. and D. Loewenthal (1972). Computer generated seismograms, in *Methods in computational physics* (Alder, Fernbach, and Rotenberg, Eds.), 12, Academic Press, 35-164.

Alterman, Z., and A. Rotenberg (1969). Seismic waves in a quarter plane, *Bull. Seism. Soc. Am.*, 59, 347-368.

Anderson, D. and B. Stump (1989). Seismic wave generation by mine blasts, in *Report GL-TR-89-0194*, Geophysics Laboratory, Hanscom AFB, MA.

Baumgardt, D. R. (1991). High frequency array studies of long range Lg propagation and the causes of L_g blockage and attenuation in the Eurasian continental craton, *Report PL-TR-91-2059(I)*, Phillips Laboratory, Hanscom Air Force base, MA.

Baumgardt, D. R. and K. A. Ziegler (1988). Spectral evidence for source multiplicity in explosions: application to regional discrimination of earthquakes and explosions, *Bull. Seism. Soc. Am.*, 78, 1773-1795.

Boore, D. (1972). Finite-difference methods for seismic wave propagation in heterogeneous materials, in *Methods in computational physics* (Alder, Fernbach, and Rotenberg, Eds.), 11, Academic Press, 1-37.

Boore, D., S. C. Harmsen, and S. Harding (1981). Wave scattering from a step change in surface topography, *Bull. Seism. Soc. Am.*, 71, 117-125.

Chapman, N. C., G. A. Bollinger, and M. S. Sibol (1992). Modeling delay-fired explosion spectra and source function deconvolution at regional distances, *Report PL-TR-92-2250*, Phillips Laboratory, Hanscom AFB, MA.

Drake, L. A. (1972). Love and Rayleigh waves in nonhorizontally layered media, *Bull. Seism. Soc. Am.*, **62**, 1241-1258.

Fuyuki, M. and Y. Matsumoto (1980). Finite-difference analysis of Rayleigh wave scattering at a trench, *Bull. Seism. Soc. Am.*, **70**, 2051-2069.

Fuyuki, M. and M. Nakano (1984). Finite-difference analysis of Rayleigh wave transmission past an upward step change, *Bull. Seism. Soc. Am.*, **74**, 893-911.

Hedlin, M. A. H., J. B. Minster, and J. A. Orcutt (1990). An automatic means to discriminate between earthquakes and quarry blasts, *Bull. Seism. Soc. Am.*, **80**, 2143-2160.

Hong, M. and L. J. Bond (1986). Application of the finite difference method in seismic source and wave diffraction simulation, *Geophys. J. R. astr. Soc.*, **87**, 731-752.

Ilan, A. (1977). Finite-difference modeling for P-pulse propagation in elastic media with arbitrary polygonal surface, *J. Geophys.*, **43**, 41-58.

Ilan, A. (1978). Stabilities of finite-difference schemes for the problem of elastic wave propagation in a quarter plane, *J. Comp. Phys.*, **29**, 389-403.

Ilan, A., L. J. Bond, and M. Spivack (1979). Interaction of a compressional impulse with a slot normal to the surface of an elastic half space, *Geophys. J. R. astr. Soc.*, **57**, 463-477.

Ilan, A., and D. Loewenthal (1976). Instability of finite difference schemes due to boundary conditions in elastic media, *Geophys. Prosp.*, **24**, 431-453.

Ilan, A., A. Ungar, and Z. Alterman (1975). An improved representation of boundary conditions in finite-difference schemes for seismological problems, *Geophys. J. R. astr. Soc.*, **43**, 727-745.

Lapidus, L., and G. Pinder (1982). *Numerical solutions of partial differential equations in science and engineering*, Wiley Interscience Publication, New York.

Levander, A. (1985). Finite-difference calculations of dispersive Rayleigh wave propagation, *Tectonophysics*, **113**, 1-30.

Marfurt, K. J. (1984). Accuracy of finite-difference and finite-element modeling of the scalar and elastic wave equations, *Geophysics*, **49**, 533-549.

Mitchell, A. R., and D. F. Griffiths (1980). *The finite difference method in partial differential equations*, John Wiley & Sons, New York.

Ohtsuki, A., H. Yamahara, and K. Harumi (1984). Effect of topography and subsurface inhomogeneity on seismic Rayleigh waves, *Earthquake Eng. and Struc. Dyn.*, **12**, 795-816.

Reamer, S. K., K.-G. Hinzen, and B. W. Stump (1992). Near-source characterization of the seismic wavefield radiated from quarry blasts, *Geophys. J. Int.*, **110**, 435-450.

Smith, G. D. (1978). *Numerical solution of partial differential equations: finite difference methods (2nd ed.)*, Clarendon Press, Oxford, England.

Smith, A. (1989). High-frequency seismic observations and models of chemical explosions: implications

for the discrimination of ripple-fired mining blasts, *Bull. Seism. Soc. Am.*, **79**, 1089-1110.

Stead, R. and D. Helmberger (1988). Numerical-analytical interfacing in two-dimensions with applications to modeling NTS seismograms, in *Scattering and Attenuation of Seismic Waves, Vol. 1*, Special issue of *Pure and Applied Geophysics*, **128**, 157-193.

Stump, B. (1988). Wave propagation issues associated with explosive sources, *10th Annual DARPA/AFGL Seismic Research Symposium, (Addendum 27-43)*, Fallbrook, CA.

Stump, B. and S. K. Reamer (1990). Physical constraints on seismic waves from chemical and nuclear explosions, *12th Annual DARPA/GL Seismic Research Symposium, 159-165*, Key West, FL.

Stump, B., S. K. Reamer, and R. E. Reinke (1988). Temporal and spatial source effects from near-surface explosions, *10th Annual DARPA/AFGL Seismic Research Symposium, 95-113*, Fallbrook, CA.

Virieux, J. (1986). P-SV wave propagation in heterogeneous media: velocity-stress finite-difference method, *Geophysics*, **51**, 889-901. .

(THIS PAGE INTENTIONALLY LEFT BLANK)

DISTRIBUTION LIST

NON-GOVERNMENT CONTRACTORS

Prof. Thomas Ahrens
Seismological Lab, 252-21
Div. of Geol. & Planetary Sciences
California Institute of Technology
Pasadena, CA 91125

Dr. Thomas C. Bache, Jr.
Dr. Thomas J. Sereno, Jr.
Science Applications Int'l Corp.
10260 Campus Point Drive
San Diego, CA 92121 (2)

Dr. Peter Basham
Dr. Robert North
Earth Physics Branch
Geological Survey of Canada
1 Observatory Crescent
Ottawa, Ontario,CANADA K1A OY3

Dr. Douglas R. Baumgardt
Dr. Zoltan A. Der
ENSCO, Inc.
5400 Port Royal Road
Springfield, VA 22151-2388

Prof. Jonathan Berger
IGPP, A-025
Scripps Institution of Oceanography
University of California, San Diego
La Jolla, CA 92093

Dr. G. A. Bollinger
Department of Geological Sciences
Virginia Polytechnic Institute
21044 Derring Hall
Blacksburg, VA 24061

The Librarian
Dr. Jerry Carter
Dr. Stephen Bratt
Center for Seismic Studies
1300 North 17th Street, Suite 1450
Arlington, VA 22209-2308 (3)

Michael Browne
Teledyne Brown Engineering
3401 Shiloh Road
Garland, TX 75041

Dr. Lawrence J. Burdick
Woodward-Clyde Consultants
566 El Dorado Street
Pasadena, CA 91109-3245

Dr. Theodore Cherry
Science Horizons, Inc.
710 Encinitas Blvd, Suite 200
Encinitas, CA 92024 (2)

Dr. Kin-Yip Chun
Geophysics Division
Physics Department
University of Toronto
Ontario, CANADA M5S lA7

Dr. Paul M. Davis
Dept. Earth & Space Sciences
University of California (UCLA)
Los Angeles, CA 90024

Prof. Steven Day
Department of Geological Sciences
San Diego State University
San Diego, CA 92182

Ms. Eva Johannisson
Senior Research Officer
National Defense Research Institute
P.O. Box 27322
S-l02 54 Stockholm, SWEDEN

Dr. Mark D. Fisk
Mission Research Corporation
735 State Street
P.O. Drawer 719
Santa Barbara, CA 93102

Prof. Stanley Flatte
Applied Sciences Building
University of California
Santa Cruz, CA 95064

Dr. Roger Fritzel
Pacific Sierra Research
l40l Wilson Blvd., Suite ll00
Arlington, VA 22209

Dr. Holly K. Given
Inst. Geophys. & Planet. Phys.
Scripps Inst. Oceanography (A-025)
University of California, San Diego
La Jolla, CA 92093

Prof. Hans-Peter Harjes
Institute for Geophysik
Ruhr University/Bochum
P.O. Box 102148
463 Bochum I, FRG

Prof. Donald V. Helmberger
Seismological Laboratory
Div. of Geol. & Planetary Sciences
California Institute of Technology
Pasadena, CA 91125

Prof. Eugene Herrin
Prof. Brian Stump
Inst. for the Study of Earth and Man
Geophysical Laboratory
Southern Methodist University
Dallas, TX 75275

Prof. Bryan Isacks
Prof. Muawia Barazangi
Cornell University
Department of Geological Sciences
SNEE Hall
Ithaca, NY 14850

Prof. Lane R. Johnson
Prof. Thomas V. McEvilly
Seismographic Station
University of California
Berkeley, CA 94720

Robert C. Kemerait
ENSCO, Inc.
445 Pineda Court
Melbourne, FL 32940

Prof. Brian L.N. Kennett
Research School of Earth Sciences
Institute of Advanced Studies
G.P.O. Box 4
Canberra 2601, AUSTRALIA

Dr. Richard LaCoss
MIT-Lincoln Laboratory
M-20 B
P.O. Box 73
Lexington, MA 02173-0073

Prof. Fred K. Lamb
Univ. of Illinois
Department of Physics
1110 West Green Street
Urbana, IL 61801

Prof. Charles A. Langston
Geosciences Department
403 Deike Building
The Pennsylvania State University
University Park, PA 16802

Prof. Thorne Lay
Dr. Susan Schwartz
Institute of Tectonics
Earth Science Board
University of California, Santa Cruz
Santa Cruz, CA 95064

Prof. Arthur Lerner-Lam
Prof. Paul Richards
Prof. C.H. Scholz
Lamont-Doherty Geol. Observatory
of Columbia University
Palisades, NY 10964

Dr. Manfred Henger
Fed. Inst. for Geosci. & Nat'l Res.
Postfach 510153
D-3000 Hanover 51, FRG

Dr. Peter Marshall
Dr. Alan Douglas
Procurement Executive
Ministry of Defense
Blacknest, Brimpton
Reading FG7-4RS, United Kingdom

Dr. Randolph Martin, III
New England Research , Inc.
76 Olcott Drive
White River Junction, VT 05001

Dr. Bernard Massinon
Societe Radiomana
27 rue Claude Bernard
75005 Paris, FRANCE (2)

Dr. Gary McCartor
Prof. Henry L. Gray
Department of Physics
Southern Methodist University
Dallas, TX 75275

Dr. Keith L. McLaughlin
S-Cubed
P.O. Box 1620
La Jolla, CA 92038-1620

Dr. Pierre Mecheler
Societe Radioman
27 rue Claude Bernard
75005 Paris, FRANCE

Prof. Bernard Minster
Prof. John Orcutt
IGPP, A-025
Scripps Institute of Oceanography
University of California, San Diego
La Jolla, CA 92093

Prof. Brian J. Mitchell
Dr. Robert Herrmann
Dept. of Earth & Atmospheric Sciences
St. Louis University
St. Louis, MO 63156

Mr. Jack Murphy
S-Cubed
11800 Sunrise Valley Drive
Suite 1212
Reston, VA 22091 (2)

Dr. Jay J. Pulli
Radix Systems, Inc.
2 Taft Court, Suite 203
Rockville, MD 20850

Dr. Frode Ringdal
Dr. Svein Mykkeltveit
NTNF/NORSAR
P.O. Box 51
N-2007 Kjeller, NORWAY (2)

Mr. Wilmer Rivers, Jr.
Teledyne Geotech Alexandria Laboratory
314 Montgomery Street
Alexandria, VA 22314-1581

Dr. Richard Sailor
TASC, Inc.
55 Walkers Brook Drive
Reading, MA 01867

Prof. Charles G. Sammis
Prof. Kei Aki
Center for Earth Sciences
University of Southern California
University Park
Los Angeles, CA 90089-0741

Prof. David G. Simpson
Lamont-Doherty Geological Observatory
of Columbia University
Palisades, NY 10964

Dr. Stewart W. Smith
Geophysics AK-50
University of Washington
Seattle, WA 98195

Prof. Clifford Thurber
Prof. Robert P. Meyer
University of Wisconsin-Madison
Department of Geology & Geophysics
1215 West Dayton Street
Madison, WS 53706

Prof. M. Nafi Toksoz
Earth Resources Lab
Mass. Institute of Technology
42 Carleton Street
Cambridge, MA 02142

Prof. Terry C. Wallace
Dept. of Geosciences
Building #77
University of Arizona
Tucson, AZ 85721

Dr. William Wortman
Mission Research Corporation
8560 Cinderbed Road
Suite 700
Newington, VA 22122

U.S. GOVERNMENT AGENCIES

Mr. Alfred Lieberman
ACDA/VI-OA, Room 5726
320 21st Street, N.W.
Washington, D.C. 20451

Colonel Jerry J. Perrizo
AFOSR/NP, Building 410
Bolling AFB
Washington, D.C. 20331-6448

Dr. Robert R. Blandford
AFTAC/CSS
1300 N. 17th Street, Suite 1450
Arlington, VA 22209

AFTAC/CA
(STINFO)
Patrick AFB, FL 32925-6001

Dr. Frank F. Pilotte
HQ AFTAC/TT
Patrick AFB, FL 32925-6001

Katie Poley
CIA-ACIS/TMC
Room 4X16NHB
Washington, D.C. 20505

Dr. Larry Turnbull
CIA-OSWR/NED
Washington, DC 20505

Dr. Ralph W. Alewine, III
Dr. Alan S. Ryall, Jr.
DARPA/NMRO
3701 N. Fairfax Drive
Arlington, VA 22303-1714 (7)

DARPA/OASB/Librarian
3701 N. Fairfax Drive
Arlington, VA 22303-1714

Dr. Dale Glover
DIA/DT-1B
Washington, D.C. 20301

Dr. Michael Shore
Defense Nuclear Agency/SPSS
6801 Telegraph Road
Alexandria, VA 22310

Dr. Max Koontz
U.S. Dept. of Energy/DP-5
Forrestal Building
1000 Independence Avenue
Washington, D.C. 20585

Defense Technical Information Center
Cameron Station
Alexandria, VA 22314 (2)

Dr. John J. Cipar, PL/GPEH
Dr. Anton W. Dainty
Phillips Lab/Geophysics Directorate
Hanscom AFB, MA 01731 (2)

James F. Lewkowicz, PL/GPEH
Phillips Lab/Geophysics Directorate
Hanscom AFB, MA 01731

Phillips Laboratory (PL/XO)
Hanscom AFB, MA 01731

Dr. James Hannon
Lawrence Livermore National Laboratory
P.O. Box 808
Livermore, Ca 94550 (2)

Office of the Secretary of Defense
DDR&E
Washington, D.C. 20330

Eric Chael
Division 9241
Sandia Laboratory
Albuquerque, NM 87185

Dr. William Leith
U.S. Geological Survey
Mail Stop 928
Reston, VA 22092

Dr. Robert Masse
Box 25046, Mail Stop 967
Denver Federal Center
Denver, CO 80225

Dr. Robert Reinke
WL/NTESG
Kirtland, AFB, NM 87117-6008

70